

Cite this: *Energy Environ. Sci.*,  
2022, 15, 3519

# Peripheral halogenation engineering controls molecular stacking to enable highly efficient organic solar cells†

Yalu Zou,<sup>‡a</sup> Hongbin Chen,<sup>‡a</sup> Xingqi Bi,<sup>a</sup> Xiaoyun Xu,<sup>b</sup> Hebin Wang,<sup>c</sup> Menglu Lin,<sup>c</sup> Zaifei Ma,<sup>‡b</sup> Mingtao Zhang,<sup>‡a</sup> Chenxi Li,<sup>a</sup> Xiangjian Wan,<sup>‡a</sup> Guankui Long,<sup>‡cd</sup> Yao Zhaoyang<sup>‡\*a</sup> and Yongsheng Chen<sup>‡\*a</sup>

The diverse molecular stacking tuned by peripheral halogens in non-fullerene acceptors (NFAs) significantly affects the molecular physicochemical properties, the film morphologies and thus the power conversion efficiencies (PCEs) of organic solar cells (OSCs). Despite the crucial role of peripheral halogens, few explorations have been performed to bridge peripheral halogenation with molecular stackings and device performances, especially for the state-of-the-art Y-series. Herein, a series of high-efficient NFAs, **CH-6F**, **CH-4Cl** and **CH-6Cl**, are constructed with the same backbone but different peripheral halogenations in both conjugate extended central units and end groups. Single-crystal analysis indicates that **CH-6F** possesses similar molecular packings to **Y6**; however, **CH-4Cl** and **CH-6Cl** with chloro-substitutions demonstrate several quite unique packing modes of end unit to central unit, etc. Compared with **CH-6F** and **Y6**, **CH-4Cl** and **CH-6Cl** possess greatly reduced electron reorganization energies and shorter intermolecular packing distances, and exhibit more balanced charge mobilities, better phase separation, and lower energy disorders when blended with the **PM6** donor. Furthermore, the reduced energy offsets between charge transfer and local exciton states for **CH-4Cl** and **CH-6Cl** result in an enhanced hybridization of these two states and thus suppress the non-radiative recombination losses in OSCs. Consequently, high-efficient OSCs are afforded by utilizing **CH**-series NFAs with a champion PCE of 18.22% and a markedly reduced  $\Delta V_{nr}$  of 0.203 V in **CH-4Cl**-based ternary devices. Our study reveals that such a slight modification of peripheral halogens could cause quite different but superior intermolecular packings, rendering peripheral halogenation engineering as an effective strategy to further boost PCEs of high-performance OSCs through delicate molecular stacking control.

Received 25th April 2022,  
Accepted 4th July 2022

DOI: 10.1039/d2ee01340a

rsc.li/ees

<sup>a</sup> The State Key Laboratory and Institute of Elemento-Organic Chemistry, Centre of Nanoscale Science and Technology, Key Laboratory of Functional Polymer Materials, Renewable Energy Conversion and Storage Center (RECAST), College of Chemistry, Nankai University, Tianjin 300071, China.

E-mail: zyao@nankai.edu.cn, yschen99@nankai.edu.cn

<sup>b</sup> The State Key Laboratory for Modification of Chemical Fibers and Polymer Materials, Center of Advanced Low-Dimension Materials, College of Materials Science and Engineering, Donghua University, Shanghai, 201620, China

<sup>c</sup> The National Institute for Advanced Materials, Renewable Energy Conversion and Storage Center (RECAST), College of Materials Science and Engineering, Nankai University, Tianjin, 300350, China

<sup>d</sup> The State Key Laboratory of Luminescent Materials and Devices, South China University of Technology, Guangzhou, 510640, China

† Electronic supplementary information (ESI) available: Experimental details are available in the online version of the paper. CCDC 2168458, 2168455 and 2168457. For ESI and crystallographic data in CIF or other electronic format see DOI: <https://doi.org/10.1039/d2ee01340a>

‡ Authors contributed equally.

## Introduction

Organic solar cells (OSCs) have attracted great attention in both academic and industrial fields due to their great advantages including solution processing, low-cost, and great potential in achieving flexible or semi-transparent devices, together with continuing increased power conversion efficiencies (PCEs).<sup>1–6</sup> Traditional electron acceptors based on fullerene have dominated OSCs for decades; however, fullerene acceptors come with several challenges such as difficulties in making chemical modifications, absorbing only high-energy photons, and unstable device performance.<sup>7,8</sup> In the last few years, non-fullerene acceptors (NFAs) have emerged and boosted the PCE of tandem OSCs towards 20% and single-junction OSCs towards 19.6% owing to their stronger and broader absorption in visible and near-infrared regions, adjustable energy levels, being easy to chemically modify, and more importantly, strong and superior molecular stacking.<sup>9–18</sup>

NFAs usually feature planar conjugated backbones and exhibit various molecular stacking and aggregation behaviors during the film casting process.<sup>19,20</sup> This can result in significantly improved exciton dissociation, charge transport and recombination, and thus a much enhanced PCE of OSCs.<sup>21–24</sup> Therefore, optimizing the phase separated feature of active layers through molecular stacking control should be the key point in further improvement of device performance. Nevertheless, how to conduct molecular structural engineering to tune the molecular stacking precisely and further afford suitable film micromorphologies still poses great challenges.

Diverse peripheral groups, especially for halogens, have been employed to modify NFAs,<sup>25–29</sup> which can result in multiple changes of molecular properties by (I) tuning the energy levels, (II) modifying the absorption spectra, (III) improving carrier mobilities, (IV) changing intermolecular interactions and crystallinity, *etc.*<sup>30–32</sup> In addition to the experimental studies above, many theoretical studies have also testified that peripheral halogenation tends to enlarge the dipole moment variations remarkably between the ground and first excited states of NFAs, which could minimize the exciton binding energy and thus improve the exciton dissociation efficiency even with a very small driving force.<sup>33,34</sup> Moreover, peripheral halogenation can simultaneously enhance molecular packing orders and crystallization, optimize film morphologies,<sup>35,36</sup> facilitate carrier mobility and decrease the resistance of the bulk heterojunction.<sup>37</sup> Among different halogenations, fluorine and chloride with large electronegativity but a small atomic radius are particularly effective in tuning the physicochemical characteristics of NFAs without introducing undesirable steric hindrance,<sup>38,39</sup> such as enhancing the intramolecular charge transfer (ICT) effects,<sup>40</sup> down-shifting molecular energy levels,<sup>41</sup> and promoting nanoscale aggregation.<sup>42</sup> In detail, the great improvement of OSC performance caused by peripheral fluorination or chlorination of NFAs could be generally attributed to two aspects. At the single-molecular level, such a halogenation could render suitable energy levels, enhance light absorption, and improve excited state lifetimes.<sup>43–46</sup> At the level of molecular aggregation, peripheral halogenation could usually enhance intermolecular interaction of NFAs, shorten  $\pi$ - $\pi$  stacking distance, and enhance molecular packing orders and crystallization, thus leading to better film morphologies and reduced energy losses in OSCs.<sup>35,36,47–50</sup> Although both experimental and theoretical studies have highlighted the irreplaceable effects of halogenation on improved PCEs of OSCs, the lack of systematical investigation, especially on the state-of-the-art Y-series NFAs, makes the connection of halogenation with molecular packings, active layer morphology, charge transfer/transport dynamics and device performances of the resulting OSCs as a crucial but still unaddressed issue.

Given the dominant molecular packing mode of end unit to end unit (E/E) observed in the single crystals of ITIC<sup>51,52</sup> and F<sup>53,54</sup> series NFAs, significantly improved photodynamic processes and even PCEs have been generally achieved after halogen substitution on the end groups.<sup>55,56</sup> However, in a typical Y6 single crystal,<sup>57–59</sup> the central unit of benzothiadiazole (BT) is also largely involved in molecular packing and leads

to a much more effective three-dimensional nanoscale network, which is significantly different from those in ITIC and F series NFAs. Based on these results, it is expected that the degree of molecular packing affected by the halogenation on central units may be no less than that of on end groups in Y-series NFAs, and further improvement of OSCs possibly could be rendered if suitable halogenation can be also conducted on central units of high-performance Y-series NFAs. Nevertheless, very few investigations have been performed thus far to unveil the crucial effects of central unit halogenation on molecular stackings, energy losses and even PCEs of OSCs in Y-series NFAs. Two reasons should account for the rare trials: (I) there are no extra reactive sites for further halogenation based on the chemical structure of the BT central unit; and (II) the construction of central heterocyclic units is very challenging when attempting to replace the BT central unit. Although facing great challenges, it is really meaningful to disclose the effects of halogenation in both central units and end groups on molecular stackings and the corresponding photovoltaic parameters, since that may make a major contribution to the optimized molecular packing modes<sup>57,58,60,61</sup> of NFAs and also the improvement of OSCs.

In this contribution, a new series of NFAs with the same benzoquinoxaline central unit<sup>62–64</sup> has been constructed by conjugated extension of the central unit, affording another two chemical active sites on the central unit. In order to reveal the significant effects of halogenation on molecular stacking, herein diverse halogen atoms were introduced at different positions alternating from end groups to central units, to manipulate the molecular packings of NFAs. Fig. 1a displays the chemical structures of NFAs studied here, ranging from the all-fluorinated CH-6F to both fluorinated and chlorinated CH-4Cl, and further all-chlorinated CH-6Cl. With CH-series NFAs, a comprehensive study has been conducted to systematically probe the significant effects of peripheral halogenation on their single crystal packings, disclosing the peripheral halogenation induced completely different crystal systems and quite unique molecular packing modes. Moreover, this superior molecular packing optimizes film morphology, improves photovoltaic performances, and reduces energy losses of the resulting OSCs, finally affording a series of high-efficient OSCs by utilizing CH-series NFAs with a champion PCE of 18.22% and a markedly reduced  $\Delta V_{nr}$  of 0.203 V in CH-4Cl-based ternary devices. Our results indicate that controlling molecular stacking modes by peripheral halogenation engineering should be a possible avenue toward OSCs with higher efficiency.

## Results and discussion

### Synthesis and characterization

The successful synthesis routes to CH-6F, CH-4Cl and CH-6Cl are displayed in Scheme S1 (ESI<sup>†</sup>) and the detailed procedures and characterization studies are described in Schemes S2–S5 and Fig. S38–S54 (ESI<sup>†</sup>). Herein, taking the synthesis of CH-6Cl

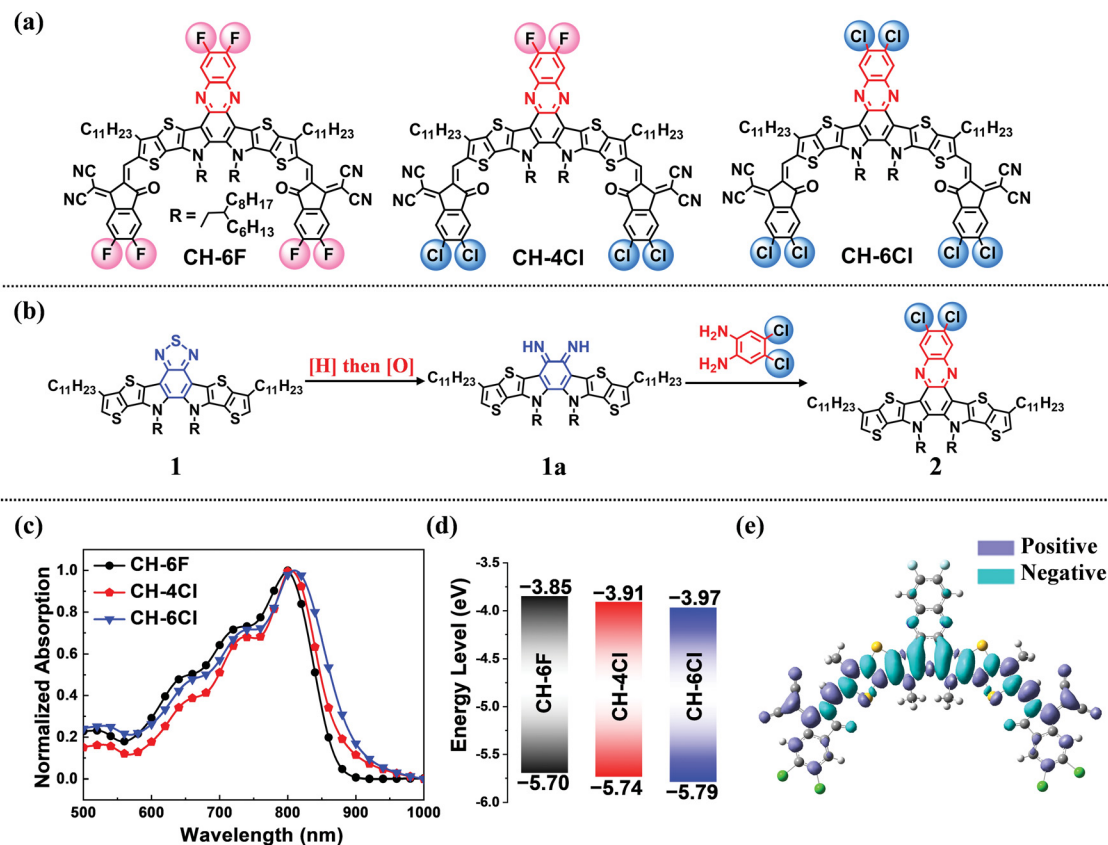


Fig. 1 Molecular structures and photophysical properties. (a) Chemical structures of **CH-6F**, **CH-4Cl**, and **CH-6Cl**. (b) Explored synthesis routes of the central unit of **CH-6Cl**. (c) Normalized absorption spectra of acceptors in neat films. (d) The energy levels of acceptors in neat films. (e) Iso-surface of charge density difference ( $\Delta Q$ ) for **CH-4Cl**, where  $\Delta Q = \Psi_{\text{LUMO}}^2 - \Psi_{\text{HOMO}}^2$ ; the positive and negative with different colors refer to  $\Delta Q > 0$  and  $\Delta Q < 0$ ,<sup>56</sup> respectively.

as an example (Fig. 1b), the indispensable but challenging step of phenazine conversion from benzothiadiazole was conducted by an *in situ* reaction in a good yield of 74%, which was developed by converting compound **1** into an intermediate diimine (**1a**) first through reduction and subsequent oxidation, further followed by an *in situ* condensation with a diamine (Note S1, ESI<sup>†</sup>). Fig. S1 (ESI<sup>†</sup>) and Fig. 1c present the normalized absorption spectra of **CH-6F**, **CH-4Cl** and **CH-6Cl** in solutions and neat films, respectively. In dilute chloroform solutions, **CH-4Cl** and **CH-6Cl** possess maximum absorption wavelengths ( $\lambda_{\text{max}}$ ) of 803 and 809 nm, bathochromically shifted by 4 and 10 nm, respectively, compared with that of 799 nm for **CH-6F** after chlorination. Moreover, the enhanced molar extinction coefficients ( $\epsilon$ ) of  $2.27 \times 10^5$  and  $2.20 \times 10^5 \text{ M}^{-1} \text{ cm}^{-1}$  can be also afforded by **CH-4Cl** and **CH-6Cl** in comparison to that of  $2.11 \times 10^5 \text{ M}^{-1} \text{ cm}^{-1}$  by **CH-6F**. From solutions to thin films, all **CH-series** NFAs exhibit an obvious red-shift ( $\sim 52 \text{ nm}$ ), demonstrating that there exists an effective intermolecular  $\pi$ - $\pi$  stacking at the solid state (Fig. 1c).<sup>65</sup> The optical bandgaps ( $E_{\text{g}}^{\text{opt}}$ ) of **CH-6F**, **CH-4Cl** and **CH-6Cl** were calculated from their thin-film absorption edge ( $\lambda_{\text{onset}}$ ) of 879, 888 and 914 nm, being 1.41, 1.39 and 1.36 eV, respectively (Table 1). The change of bandgaps should be ascribed to the variations of energy levels induced by diverse peripheral halogenations. Therefore, cyclic voltammetry

Table 1 The optical and electrochemical properties of CH-series NFAs

NFAs	$\lambda_{\text{max}}^{\text{cf}}$ (nm)	$\lambda_{\text{max}}^{\text{film}}$ (nm)	HOMO (eV)	LUMO (eV)	$E_{\text{g}}^{\text{cv}}$ (eV)	$\lambda_{\text{onset}}^{\text{film}}$ (nm)	$E_{\text{g}}^{\text{opt}}$ (eV)	$\epsilon$ ( $10^5 \text{ M}^{-1} \text{ cm}^{-1}$ )
<b>CH-6F</b>	742	799	-5.70	-3.85	1.85	879	1.41	2.11
<b>CH-4Cl</b>	756	803	-5.74	-3.91	1.83	888	1.39	2.27
<b>CH-6Cl</b>	755	809	-5.79	-3.97	1.82	914	1.36	2.20

<sup>a</sup> In the chloroform solution. <sup>b</sup> In a neat film. <sup>c</sup>  $E_{\text{g}}^{\text{cv}} = E_{\text{LUMO}} - E_{\text{HOMO}}$ . <sup>d</sup>  $E_{\text{g}}^{\text{opt}} = 1240/\lambda_{\text{onset}}^{\text{film}}$ .

(CV) was performed to evaluate the energy levels of **CH-6F**, **CH-4Cl** and **CH-6Cl** (Fig. 1d and Fig. S2, ESI<sup>†</sup>). Based on the oxidation and reduction onsets, the highest occupied molecular orbital (HOMO) and the lowest unoccupied molecular orbit (LUMO) energy levels can be estimated to be  $-5.70$  and  $-3.85 \text{ eV}$  for **CH-6F**,  $-5.74$  and  $-3.91 \text{ eV}$  for **CH-4Cl**, and  $-5.79$  and  $-3.97 \text{ eV}$  for **CH-6Cl**. Although fluorine has a larger electronegativity than a chlorine atom, the enhanced electron-donating p- $\pi$  conjugation of fluorine atoms with the broad conjugated backbone of NFAs enables the upshifted LUMO/HOMO of **CH-6F** compared to those of **CH-4Cl** and **CH-6Cl**. Note that a similar tendency has also been observed from the DFT calculations shown in Fig. S3 (ESI<sup>†</sup>). The derived energy gaps from CV measurements for **CH-6F**, **CH-4Cl** and **CH-6Cl** can be

determined to be 1.85, 1.83 and 1.82 eV, respectively, which agree well with their optical bandgaps.

The thermal stability of CH-series NFAs was investigated by thermogravimetric analysis (TGA). As displayed in Fig. S4 (ESI<sup>†</sup>), all the three NFAs exhibit excellent thermal stability at decomposition temperatures of 332, 329 and 332 °C for CH-6F, CH-4Cl and CH-6Cl, respectively, at a 5% weight loss. In addition, a clear acceptor–donor–acceptor (A–D–A) feature for the three NFAs can be indicated by the characteristic peak–valley–peak plots along the longest direction of the molecular backbone (Fig. 1e and Fig. S5, ESI<sup>†</sup>) for their frontier orbital charge density difference ( $\Delta Q$ ).<sup>66</sup> As it has been proposed before, such a unique feature with a peak–valley–peak plot of  $\Delta Q$  for A–D–A type NFAs will enhance their molar extinction coefficient, facilitate better exciton separation and charge transport, and thus lead to better performance OSCs with small energy losses compared with some other types of molecules.

### Molecular packing in single crystals

As we have discussed above, different peripheral halogenations in NFAs could have a significant effect on molecular stacking.

Therefore, single-crystal X-ray diffraction measurements of CH-6F, CH-4Cl and CH-6Cl were performed first to investigate the molecular geometry and stacking mode variations caused by diverse peripheral halogenations. The needle-like single crystals with a reddish-brown metallic luster for CH-series NFAs were grown in chloroform by a slow solvent diffusion method using *n*-hexane or methanol as the antisolvents (see the experimental section for details, ESI<sup>†</sup>). The related parameters of CH-6F, CH-4Cl and CH-6Cl crystals are listed in Table S1 (ESI<sup>†</sup>) and those of Y6 were obtained from the literature.<sup>57,58</sup> As illustrated in Fig. 2a–d, all CH-series NFAs exhibit a similar banana-curved and helical molecular geometry to that of Y6. Among them, CH-6F and Y6 both have two configurations (Fig. S6, ESI<sup>†</sup>), whereas CH-4Cl and CH-6Cl have only one configuration. Note that the fewer conformations of CH-4Cl and CH-6Cl should be conducive to the more ordered molecular stacking and lower energetic disorder which will be discussed below. More interestingly, the molecular torsion angle consisting of planes built from the two end groups is 3.1° for CH-6F, 2.8° for CH-4Cl and 18.5° for CH-6Cl, all much smaller

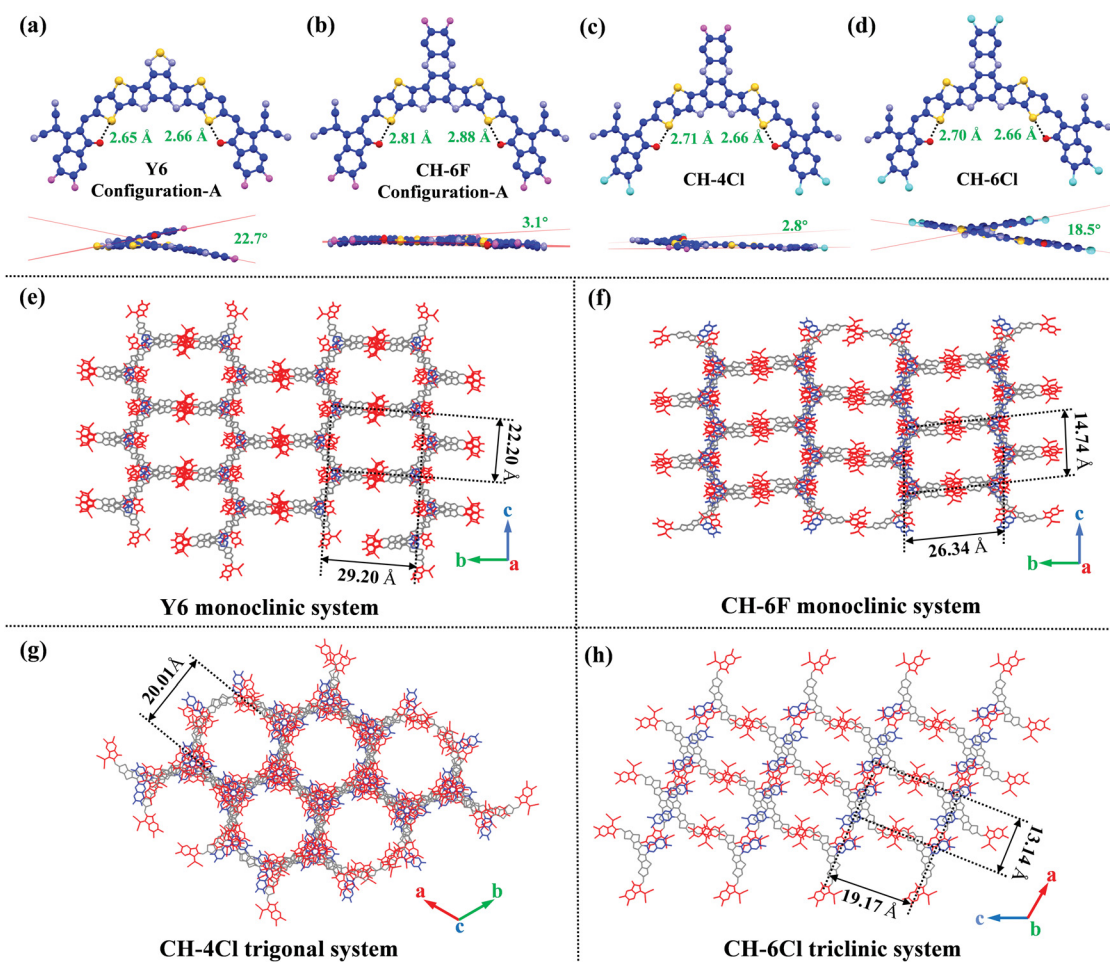


**Fig. 2** Single-crystal structures of Y6, CH-6F, CH-4Cl and CH-6Cl. (a–d) Monomolecular single crystallographic structures in top-view ( $d_{S-O}$  = the length of the S...O interaction) and side-view (the alkyl chains and hydrogen atoms are omitted for clarity) and (e–h) single-crystal packing diagrams from the top view of Y6, CH-6F, CH-4Cl, and CH-6Cl. Red: end groups (E), grey: bridge unit (b), and blue: central unit (C). Y6 and CH-6F both have two configurations and all configurations have been extracted in Fig. S6 (ESI<sup>†</sup>) and other views of indicated crystals are displayed in Fig. S8–S11, ESI<sup>†</sup>.

than that of 22.7° for **Y6**. This is consistent with the observed stronger non-covalent S–N secondary interaction between the central unit and bridged thiophene with a van der Waals distance of  $\sim 3.30$  Å formed only in the **CH**-series NFA molecules (the non-bonding S–N distance is  $\sim 3.50$  Å,<sup>67</sup> Fig. S7, ESI†). The relatively larger torsion angle of **CH-6Cl** with respect to those of **CH-6F** and **CH-4Cl** may be caused by the larger atomic radius of chlorine atoms on the central units. The extended conjugated backbones in combination with their unique S–N non-covalent secondary interactions enhance the planarity and rigidity of **CH**-series NFAs greatly, which could theoretically lead to a reduction of electron reorganization energies ( $\lambda$ ).<sup>58,68</sup> As can be expected, the calculated  $\lambda$  values for **CH-6F**, **CH-4Cl** and **CH-6Cl** are 145.5, 135.4 and 136.6 meV, respectively, smaller than that of 148.0 meV for **Y6** (Table 1). The smaller  $\lambda$  may render **CH**-series NFAs as better charge transport materials than **Y6** based on Marcus charge-transfer theory.<sup>69</sup>

As we have mentioned above, not only end groups but also central units can effectively participate in the compact molecular stackings in **Y**-series NFAs, that is why peripheral halogenations on both end groups and central units have been performed in this work. As shown in Fig. 2e–h, different peripheral halogenations indeed result in dramatically different single crystal structures for **CH**-series NFAs. In the reported **Y6** single crystal, which belongs to a monoclinic system,<sup>57,58</sup> the central unit plays a unique role in constructing the three-dimensional (3D) network with rectangle-shaped voids of  $\sim 22.2 \times 29.2$  Å. From **Y6** to **CH-6F** with an extended central unit but the same fluorinated terminals, the single crystal of **CH-6F** could also be attached to the monoclinic system with similar rectangle-shaped voids. However, **CH-6F** forms much smaller voids of  $\sim 14.7 \times 26.3$  Å than **Y6**, which should be caused by the  $\pi$ -conjugated extension of central units. When substituting the peripheral fluorine atoms on the terminals of **CH-6F** with chlorine atoms, the single crystal of **CH-4Cl** exhibits a dramatically changed crystalline system of trigonal and a small circle-shaped void with a diameter of  $\sim 20.0$  Å. Further replacing the fluorines on the central units with chlorides, the crystalline system for **CH-6Cl** single crystal continues to transform into a triclinic system with rectangle-shaped voids of  $\sim 13.1 \times 19.2$  Å. As we expected, such a little modification of peripheral halogens on the same backbone significantly affects the corresponding crystalline systems and the multi-dimensionally intermolecular stacking networks, which may also have an influence on charge transfer/transport dynamics in active layers.

Intrinsically, the significant differences of crystal frameworks discussed above in the crystals of related NFAs should be caused by different peripheral halogenations and thus diverse intermolecular packing modes. Therefore, all the packing modes with intermolecular potentials  $> |70|$  kJ mol<sup>-1</sup> are shown in Fig. 3 and Fig. S12 (ESI†). From the single-crystal data shown in Fig. 3a–d, both **Y6** and **CH-6F** possess four similar packing modes, including end unit to end unit (“E/E” mode), dual end unit to bridge unit (“dual E/b” mode), end unit to end unit and central unit to central unit (“E/E + C/C” mode), which

account for their same monoclinic crystal system. After chlorination on the end groups, **CH-4Cl** maintains a similar “E/E” mode to **CH-6F**, whereas displays another newly observed distinctive mode of dual end unit to central unit (“dual E/C” mode) (Fig. 3f). With further chlorination on the central unit, the common packing mode of “E/E” mode in **Y6** and **CH-6F** can be also observed in **CH-6Cl**; nevertheless, another two different packing modes of dual central unit to bridge unit (“dual C/b” mode) and end unit to central unit (“E/C” mode) emerged (Fig. 3h). In general, compared to the four packing modes in both **Y6** and **CH-6F**, the simplified molecular packing modes of **CH-4Cl** and **CH-6Cl** may result in more ordered molecular packing, lower energetic disorders and thus reduced non-radiative recombinations. As is known, the unique “E/E + C/C” mode was first observed in **Y6** series NFAs and plays probably the most essential role in forming their 3D packing network in single crystals.<sup>57</sup> Although **CH-6F** also displays the four similar packing modes to **Y6**, its “E/E + C/C” packing mode exhibits a larger molecular packing overlap because of the extended central unit, leading to a much enlarged intermolecular potential of 236.4 kJ mol<sup>-1</sup> and closer packing distance of 3.35 Å than that of 198.6 kJ mol<sup>-1</sup> and 3.37 Å for **Y6** as displayed in Fig. 3a, 3c and Table 2. With peripheral chlorinations, the packing modes of **CH-4Cl** and **CH-6Cl** have been greatly changed and simplified. Among them, the “E/E-2” mode in **CH-6Cl** affords a greatly enlarged intermolecular potential of 140.9 kJ mol<sup>-1</sup> with respect to that of 85.5 kJ mol<sup>-1</sup> for the same mode in **CH-6F**. More importantly, the newly formed packing modes of “dual C/b” and “E/C” also present relatively large intermolecular potentials of 194.5 and 86.3 kJ mol<sup>-1</sup>, respectively, indicating strong intermolecular interactions and possibly leading to a more efficient charge transport for **CH-6Cl**. As for that of **CH-4Cl**, the “E/C” mode in **CH-6Cl** transforms into the “dual E/C” mode which possesses a much increased molecular packing overlap. The  $\pi$ – $\pi$  packing distance of **CH-4Cl** in the “dual E/C” mode can be estimated to be 3.22/3.25 Å, significantly smaller than not only 3.46 Å for “E/C” in **CH-6Cl** but also  $\sim 3.35$  Å for the other effective packing modes in **Y6** and **CH-6F**. The small  $\pi$ – $\pi$  packing distance in combination with the sufficient molecular packing overlap for the quite unique “dual E/C” mode in **CH-4Cl** contributes to a large intermolecular potential of 207.7 kJ mol<sup>-1</sup>. Therefore, it is expected that **CH-4Cl** based thin films may render an improved charge transport property when taking the only two packing modes and the efficient “dual E/C” mode into consideration.

The different peripheral halogenations on **CH**-series NFAs have led to diverse intermolecular packing modes and completely changed molecular packing networks, which should have an influence on the charge transport properties of the resulting thin films inevitably. Therefore, the hole transfer integral ( $V_{\text{H}}$ ) and electron transfer integral ( $V_{\text{E}}$ ) were calculated to evaluate the overall charge transport capacities.<sup>58,68</sup> As illustrated in Table 2, compared with **Y6**, especially in the effective “E/E + C/C” mode, **CH-6F** possesses a more effective  $V_{\text{E}}$  of 95.38 meV, which is almost comparable with that of some most well-known n-type semiconductors such as perylene diimide.<sup>70</sup>

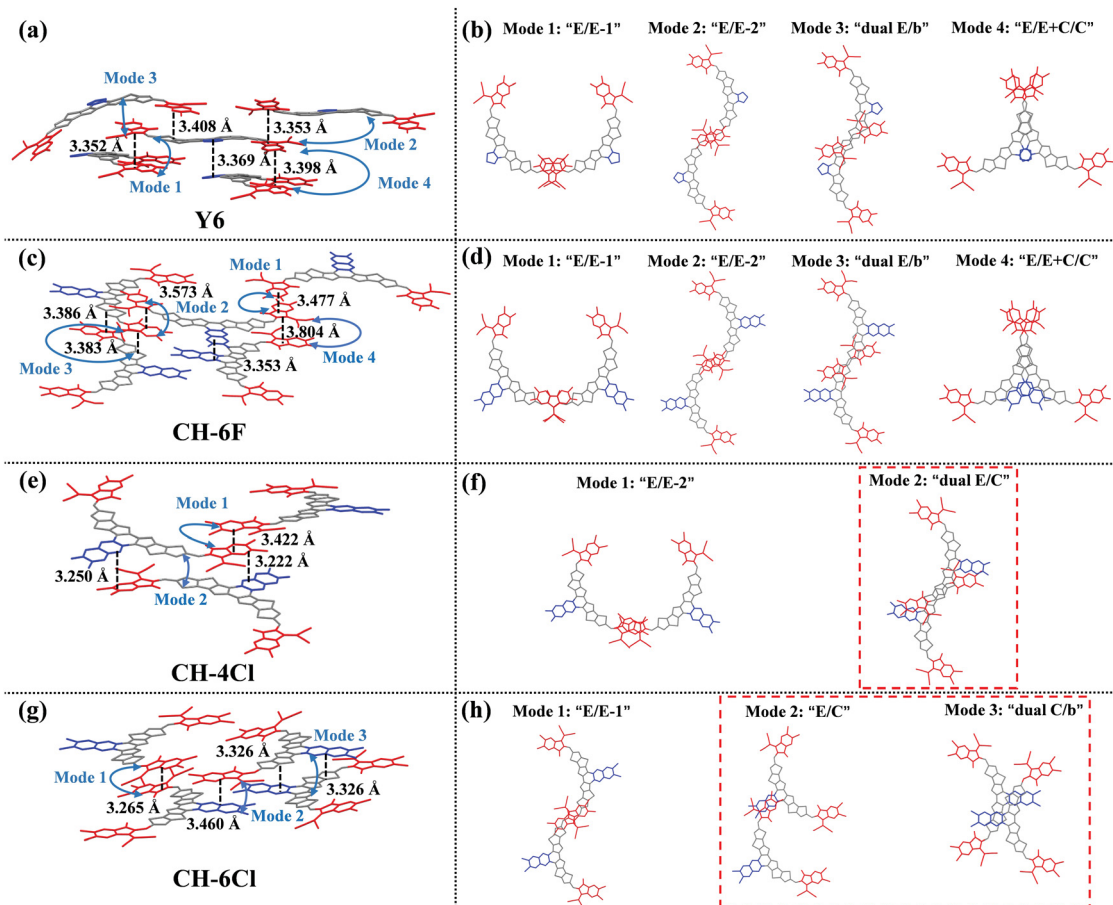


Fig. 3 Intermolecular packing modes of **Y6**, **CH-6F**, **CH-4Cl** and **CH-6Cl**. (a, c, e, g) Interlayer  $\pi$ - $\pi$  distance between acceptor molecular layers including the corresponding intermolecular packing modes and (b, d, f, h) different intermolecular packing modes of the studied NFAs. All the packing modes with UNI intermolecular potentials ( $>|70|$  kJ mol $^{-1}$ ) have been extracted (Fig. S12, ESI $^\dagger$ ).

After replacing peripheral fluorines with chlorides in **CH-6Cl**, both very small  $V_H$  and  $V_E$  can be observed for the two unique packing modes of “dual C/b” and “E/C”, rendering probably the “E/E-2” mode with a  $V_H$  of 19.85 meV and a  $V_E$  of 54.82 meV as the most effective charge transfer channel in **CH-6Cl**. But for **CH-4Cl**, the newly emerged “dual E/C” mode shows a large  $V_H$  of 52.88 meV and a  $V_E$  of 34.34 meV, which could result in both efficient and balanced hole and electron transport.<sup>70</sup> Note that the values of  $V_H$  and  $V_E$  are really hard to compare directly between different packing modes; the ratio of hole/electron transfer integral in the most effective packing modes could be applied to assess the charge transport capabilities of A–D–A acceptors.<sup>69</sup> Although all the four NFAs have demonstrated both large  $V_H$  and  $V_E$  in their preferable packing modes, **CH-4Cl** affords the most balanced electron/hole transfer integral ratio  $(V_E/V_H)^2$  of 0.42 compared to that of 1.59 for **Y6**, 5.70 for **CH-6F** and 8.59 for **CH-6Cl**, suggesting its better charge transport behaviors. As a result, due to the large and balanced transfer integral along with the smallest reorganization energy for **CH-4Cl**, the neat film of **CH-4Cl** contributes to the highest and most balanced experimental electron and hole mobility of  $3.79 \times 10^{-4}$  and  $2.06 \times 10^{-4}$  cm $^2$  V $^{-1}$  s $^{-1}$ , respectively, with

respect to those of other three NFAs (Table 2 and Fig. S18, ESI $^\dagger$ ). These results indicate that the packing mode of NFAs, including stacking distances, intermolecular potentials, and charge transfer integrals, plays a significant role in the charge transfer/transport dynamic of acceptor films, and further demonstrates the effectiveness of peripheral halogenation in controlling molecular packings and even the charge transfer/transport dynamics of NFAs.

### Photovoltaic properties

The diverse intermolecular packing networks for **CH**-series NFAs should result in different photovoltaic parameters. Therefore, OSCs with a conventional device structure (Fig. 4a) were fabricated to evaluate the potential photovoltaic performance of **CH-6F**, **CH-4Cl** and **CH-6Cl**. For the sake of complementary absorption and matched energy levels, polymer donor **PM6** has been selected to blend with NFAs studied here (Fig. S13b, ESI $^\dagger$ ). All the device optimization and the corresponding photovoltaic parameters are summarized in Tables S6–S19 (ESI $^\dagger$ ). Among them, the  $J$ - $V$  curves and device parameters of champion OSCs are presented in Fig. 4b and Table 3, respectively. Meanwhile, excellent device reproducibility can be noticed as shown in

Table 2 Crystallographic and  $\pi$ - $\pi$  interaction parameters of the studied NFAs

Comp.	Void sizes (shapes)	Packing modes	$d_{\pi-\pi}^b$ (Å)	Intermolecular-potentials (kJ mol <sup>-1</sup> )	$V_H^c$ (meV)	$V_E^d$ (meV)	Config. <sup>e</sup>	$d_{S-O}^f$ (Å)	$\lambda^g$ (meV)	$\mu_h/\mu_e^h$ (10 <sup>-4</sup> cm <sup>2</sup> V <sup>-1</sup> s <sup>-1</sup> )
<b>Y6<sup>a</sup></b>	29.2 × 22.2 Å (rectangle)	Mode1 (E/E-1)	3.352	90.1	9.69	9.53	A	2.65/2.66	148.0	1.55/1.89
		Mode 2 (E/E-2)	3.353	91.3	9.87	34.54				
		Mode 3 (Dual E/b)	3.408	178.8	81.40	10.33	B	2.60/2.67		
		Mode 4 (E/E + C/C)	3.369/3.398	198.6	31.98	40.34				
<b>CH-6F</b>	26.3 × 14.7 Å (rectangle)	Mode1 (E/E-1)	3.477	77.8	3.79	60.89	A	2.81/2.88	145.5	1.60/1.97
		Mode 2 (E/E-2)	3.573	85.5	8.62	7.04				
		Mode 3 (Dual E/b)	3.383	169.7	38.79	15.99	B	2.79/2.90		
		Mode 4 (E/E + C/C)	3.353/3.804	236.4	39.94	95.38				
<b>CH-4Cl</b>	20.0 Å (circle)	Mode1 (E/E-1)	3.422	77.6	5.09	20.25	A	2.71/2.66	135.4	2.06/3.79
		Mode 2 (Dual E/C)	3.220/3.250	207.7	52.88	34.34				
<b>CH-6Cl</b>	13.1 × 19.2 Å (rectangle)	Mode 1 (E/E-2)	3.265	140.9	19.85	54.82	A	2.70/2.66	136.6	1.65/2.76
		Mode 2 (E/C)	3.460	86.3	5.78	0.02				
		Mode 3 (Dual C/b)	3.326/3.326	194.5	11.02	0.10				

<sup>a</sup> Crystal structure of **Y6** was obtained from previously reported work.<sup>37,38</sup> <sup>b</sup>  $d_{\pi-\pi}$  is the  $\pi$ - $\pi$  interlayer distance including the main types of intermolecular packing modes of **Y6**, **CH-6F**, **CH-4Cl** and **CH-6Cl**, which is consistent with that of Fig. 3. <sup>c</sup>  $V_E$  is the electron transfer integral.

<sup>d</sup>  $V_H$  is the hole transfer integral of the corresponding packing modes. The detailed calculation methods are described in Note S2 (ESI<sup>†</sup>). <sup>e</sup> Config. represents configurations in crystals of **Y6** and **CH-6F**. <sup>f</sup>  $d_{S-O}$  represents the distance between the S atom in bridged thiophene and the O atom in a central unit. The S-O distances are also marked in Fig. 2. <sup>g</sup>  $\lambda$  represents the electron reorganization energy. <sup>h</sup> Electron and hole mobility in an optimized neat film of indicated acceptors was measured by the SCLC method, shown in Fig. S18 (ESI<sup>†</sup>).

Fig. 4d. The **CH-6F**-based device presents a superior PCE of 16.77% to 16.27% of the controlled **Y6**-based device (Table 2 and Fig. S16, ESI<sup>†</sup>), along with a  $J_{SC}$  of 25.31 mA cm<sup>-2</sup> and a high  $V_{OC}$  of 0.872 V. Notably, the **CH-4Cl**-based device yields an impressive PCE of up to 17.72% with an enhanced  $J_{SC}$  of 26.50 mA cm<sup>-2</sup> comparing to that of **CH-6F**, which could be attributed to the red-shifted absorption of **CH-4Cl**. Note that a comparable  $V_{OC}$  of 0.872 V can be achieved by **CH-4Cl**-based OSCs despite the smaller bandgap of **CH-4Cl**, indicating the possible reduced non-radiative energy loss based on the energy-gap-law.<sup>71</sup> A slightly lower PCE of 17.22% is afforded by **CH-6Cl**-based OSCs mainly due to their inferior  $V_{OC}$  and  $J_{SC}$  compared to those of the **CH-4Cl**-based one. Generally, all the three OSCs based on **CH**-series NFAs exhibit higher PCEs than **Y6**-based OSCs mainly benefitting from their enlarged  $V_{OC}$  and FF. Among them, the increased  $V_{OC}$  matches well with the gradually increased LUMO energy levels and higher FF should be ascribed to the better molecular stackings of **CH**-series NFAs. The external quantum efficiency (EQE) spectra of the devices were measured and are presented in Fig. 4c. **PM6:CH-4Cl** and **PM6:CH-6Cl**-based OSCs show a broader and higher photocurrent response than that based on **PM6:CH-6F**, which should be attributed to their red-shifted absorption and improved photodynamics discussed below. The calculated current densities obtained from the corresponding EQE curves are 24.97, 25.76 and 25.57 mA cm<sup>-2</sup> for **PM6:CH-6F**, **PM6:CH-4Cl** and **PM6:CH-6Cl**-based OSCs, respectively, which represent less than 3% mismatch with the  $J_{SC}$  values from the  $J$ - $V$  curves. We also select **D18** donor<sup>72</sup> with a lower-lying HOMO to match **CH**-series NFAs, and a higher  $V_{oc}$  of approaching 0.900 V could be afforded as we expected (Fig. S17, Tables S2 and S17–S19, ESI<sup>†</sup>). However, the inferior  $J_{SC}$  and FF lead to slightly lower PCEs compared to those of **PM6**-based OSCs.

To further understand the charge generation and dissociation behavior in OSCs, the plots of photocurrent density ( $J_{ph}$ ) versus effective voltage ( $V_{eff}$ ) were measured under short-circuit conditions and are shown in Fig. 4e, Fig. S21 and S22 (ESI<sup>†</sup>). The corresponding exciton dissociation efficiencies ( $\eta_{diss}$ ) and charge collection efficiency ( $\eta_{coll}$ ) can be afforded (see the explanation in Fig. S20 for details, ESI<sup>†</sup>). The derived  $\eta_{diss}$  values for **PM6:CH-6F**, **PM6:CH-4Cl**, **PM6:CH-6Cl** and **PM6:Y6** are 97.8%, 98.0%, 97.9% and 96.8%, respectively. The  $\eta_{coll}$  values of **PM6:CH-6F**, **PM6:CH-4Cl**, **PM6:CH-6Cl** and **PM6:Y6**-based devices can be determined to be 87.4%, 88.4%, 87.6% and 86.5%, respectively. Note that all the devices here show excellent  $\eta_{diss}$  and  $\eta_{coll}$ , whereas the slightly higher  $\eta_{diss}$  and  $\eta_{coll}$  values for **PM6:CH**-series suggest that **CH**-series NFA based devices exhibit more effective exciton dissociation and charge collection than those based on **Y6**. Then charge recombination behaviors of OSCs were evaluated by exploring the relationships between  $J_{SC}/V_{OC}$  and light intensity ( $P_{light}$ ). Under different  $P_{light}$  values, the corresponding  $J_{SC}$  follows the equation  $J_{SC} \propto (P_{light})^\alpha$ . The value of  $\alpha$  is close to the unit, indicating weak bimolecular recombination. As illustrated in Fig. S19 (ESI<sup>†</sup>), the recombination parameters ( $\alpha$ ) are 0.985, 0.988, 0.987 and 0.982 for **CH-6F**, **CH-4Cl**, **CH-6Cl** and **Y6**-based devices, respectively, suggesting quite a low degree of bimolecular recombination for all the devices. In addition, the relationships between  $V_{OC}$  and  $\ln(P_{light})$  could suggest the possibility of trap-assisted recombination. As demonstrated in Fig. 4f and Fig. S20 (ESI<sup>†</sup>), the slopes for **CH-6F**-, **CH-4Cl**- and **CH-6Cl**-based OSCs are 1.17  $kT/q$ , 1.12  $kT/q$ , and 1.15  $kT/q$ , respectively, which are slightly lower than that of **Y6**-based device (1.21  $kT/q$ ). The smaller slopes for **CH**-series NFA based devices indicate that the trap-assisted recombination has been suppressed, thus contributing to their higher FFs. All the related parameters have been summarized in Table S3 (ESI<sup>†</sup>) for a clear comparison.

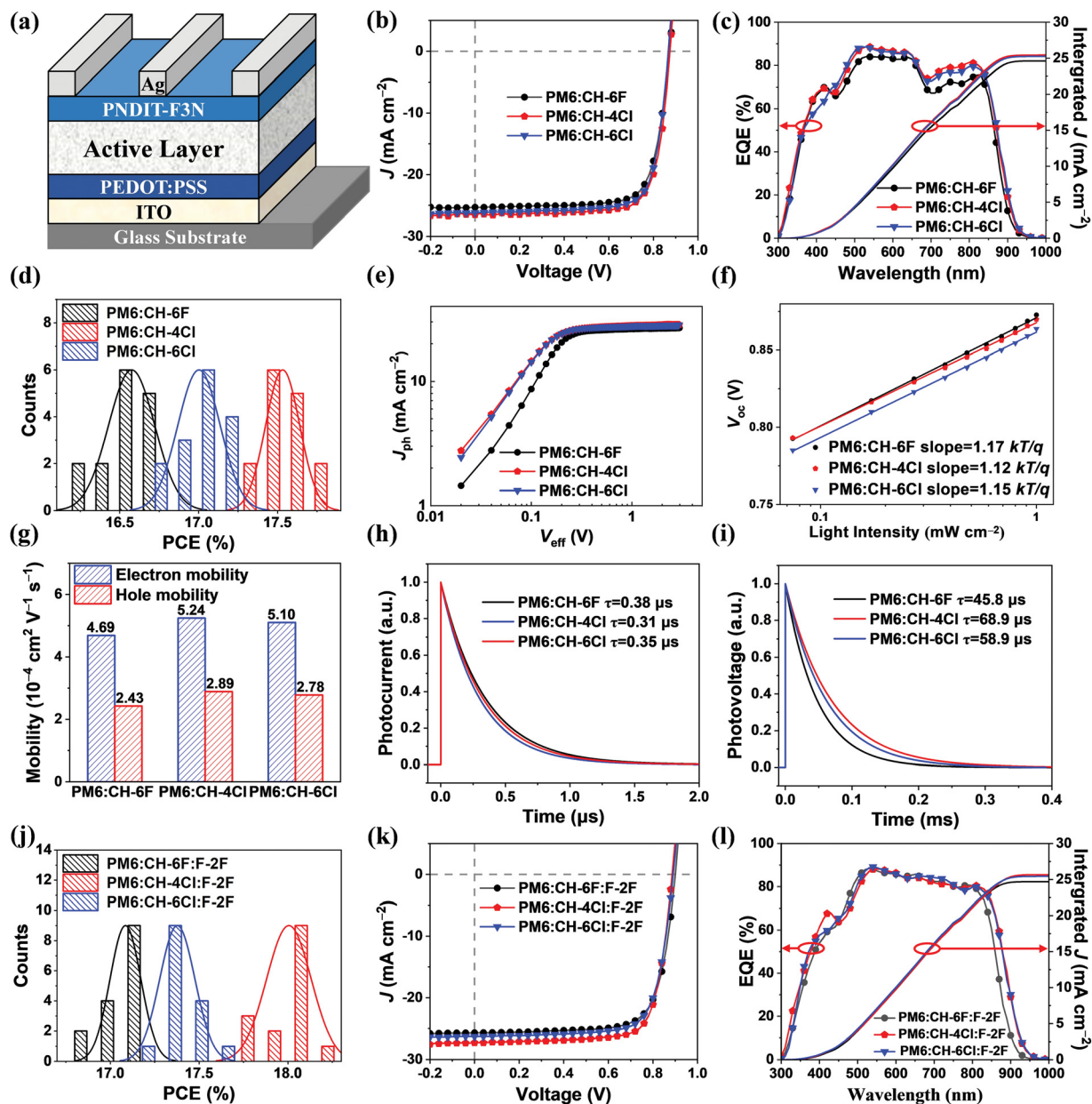


Fig. 4 Photovoltaic performances of the optimized **PM6:CH-6F**, **PM6:CH-4Cl** and **PM6:CH-6Cl** binary and ternary blend devices. (a) Solar cell device structure. (b) Current density–voltage curves. (c) EQE spectra and integral  $J_{SC}$  values. (d) PCE distributions are derived from 15 devices. (e)  $J_{ph}$  versus  $V_{eff}$  curves. (f) Light intensity ( $P_{light}$ ) dependence of  $V_{OC}$ . (g) Histograms of the electron mobility ( $\mu_e$ ) and hole mobility ( $\mu_h$ ). (h) Transient photocurrent (TPC) and (i) transient photovoltage (TPV) measurements of the devices based on **PM6:CH-6F**, **PM6:CH-4Cl** and **PM6:CH-6Cl**. The TPV and TPC measurements were performed under a white bias light with light intensity of about 0.5 sun and a diode pumped laser passing through an attenuator with light intensity of about 1132.5  $\mu\text{W cm}^{-2}$ . (j) Current density–voltage curves. (k) EQE spectra and integral  $J_{SC}$  values. (l) PCE distributions are derived from 15 devices based on **PM6:CH-6F:F-2F**, **PM6:CH-4Cl:F-2F**, and **PM6:CH-6Cl:F-2F**. F-2F<sup>53</sup> is the third component introduced in the **PM6:CH**-series-based devices in Fig. 4a and its structure and energy level are shown in Fig. S13a and c, ESI†

The charge transport properties in the optimal devices were measured by the space-charge-limited current (SCLC) method using the hole-only and electron-only devices, respectively (Fig. 4g and Fig. S18, ESI†). The calculated electron/hole mobilities for **PM6:CH-6F**, **PM6:CH-4Cl**, **PM6:CH-6Cl** and **PM6:Y6** are  $4.69 \times 10^{-4}/2.43 \times 10^{-4}$ ,  $5.24 \times 10^{-4}/2.89 \times 10^{-4}$ ,  $5.10 \times 10^{-4}/2.78 \times 10^{-4}$  and  $4.02 \times 10^{-4}/2.01 \times 10^{-4}$   $\text{cm}^2 \text{V}^{-1} \text{s}^{-1}$ , respectively, with the corresponding  $\mu_e/\mu_h$  ratios of 1.94, 1.81, 1.83 and

2.00. **CH**-series NFA based devices exhibit higher and more balanced charge mobilities than those based on **Y6**, which is consistent with the calculated mobilities derived from their single crystals. Moreover, Fig. 4h, i and Fig. S21, S22 (ESI†) show the transient photovoltage and photocurrent (TPV and TPC) decay kinetics of these devices. The **PM6:CH**-series NFA based devices showed the charge sweep-out times of 0.38  $\mu\text{s}$  for **CH-6F**, 0.31  $\mu\text{s}$  for **CH-4Cl**, and 0.35  $\mu\text{s}$  for **CH-6Cl**, slightly

Table 3 The optimal photovoltaic parameters of the studied OSCs under AM 1.5G illumination (100 mW cm<sup>-2</sup>)

Active layer	$V_{OC}$ (V)	$J_{SC}^a$ (mA cm <sup>-2</sup> )	Calc. $J_{SC}^b$ (mA cm <sup>-2</sup> )	FF <sup>a</sup> (%)	PCE <sup>a</sup> (%)
<b>PM6:Y6</b> <sup>c</sup>	0.852 (0.850 ± 0.002)	25.91 (25.82 ± 0.26)	25.04	73.72 (73.28 ± 0.73)	16.27 (16.09 ± 0.15)
<b>PM6:CH-6F</b>	0.872 (0.874 ± 0.002)	25.31 (25.13 ± 0.34)	24.97	75.99 (75.52 ± 0.68)	16.77 (16.58 ± 0.14)
<b>PM6:CH-6F:F-2F</b> <sup>d</sup>	0.900 (0.897 ± 0.002)	25.69 (25.76 ± 0.17)	25.04	74.48 (73.91 ± 0.62)	17.22 (17.09 ± 0.08)
<b>PM6:CH-4Cl</b>	0.872 (0.871 ± 0.001)	26.50 (26.49 ± 0.16)	25.76	76.68 (75.94 ± 0.41)	17.72 (17.53 ± 0.11)
<b>PM6:CH-4Cl:F-2F</b> <sup>d</sup>	0.896 (0.894 ± 0.003)	26.69 (26.50 ± 0.19)	26.01	76.17 (75.99 ± 0.40)	18.22 (18.00 ± 0.12)
<b>PM6:CH-6Cl</b>	0.866 (0.865 ± 0.003)	26.07 (26.03 ± 0.15)	25.57	76.28 (75.49 ± 0.57)	17.22 (17.00 ± 0.13)
<b>PM6:CH-6Cl:F-2F</b> <sup>d</sup>	0.892 (0.890 ± 0.001)	26.34 (26.08 ± 0.16)	25.77	74.79 (74.87 ± 0.37)	17.57 (17.38 ± 0.10)

<sup>a</sup> Optimal and statistical results are listed outside of parentheses and in parentheses, respectively. The average parameters were calculated from 15 independent devices. <sup>b</sup> Current densities calculated from EQE curves. <sup>c</sup> Photovoltaic performance of optimized **PM6:Y6** is shown in Fig. S16 (ESI).

<sup>d</sup> **F-2F** is the third component introduced in the **PM6:CH**-series-based devices in Fig. 4 below and its structure and energy level are shown in Fig. S13, ESI.

shorter than that of 0.45 μs for **Y6**. Moreover, the carrier lifetimes calculated from the TPV measurements were 45.8, 68.9, and 58.9 μs for **CH-6F**, **CH-4Cl** and **CH-6Cl** based devices, respectively, which are larger than 42.8 μs of the **Y6**-based one. The relatively shorter charge extraction time under short-circuit conditions and a higher lifetime of carriers at open-circuit voltage are correlated to the observed higher electron mobility and the weaker recombination in the **CH**-series based devices. All these results contribute to the improved  $J_{SC}$  and FF for the **CH**-series-based devices, leading to high performances of the studied OSCs. Note that among all the three **CH**-series NFAs, the **CH-4Cl** based device displays the smallest charge extraction time and largest carrier lifetime, which is consistent with its best device performances.

For **Y**-series, it has been widely observed that ternary devices have further improved OSC performances due to enhanced  $J_{SC}$ ,  $V_{OC}$  and FF, better morphology and improved light harvesting.<sup>73–80</sup> Therefore, based on these studies, we further investigate ternary devices of the **CH**-series and select **F-2F**<sup>53</sup> (Fig. S13a, ESI<sup>†</sup>) as the third component to fabricate ternary devices using the same conditions as those of the corresponding binary devices. The photovoltaic performance parameters and  $J$ - $V$  curves of the best devices are collated in Fig. 4j and k, respectively. After optimizing the ratio of the acceptors (Tables S9 and S14, ESI<sup>†</sup>), the **PM6:CH-4Cl:F-2F** (1:0.9:0.3) based ternary device exhibits the best PCE of 18.22%, resulting from the simultaneously enhanced  $V_{OC}$  of 0.896 V,  $J_{SC}$  of 26.69 mA cm<sup>-2</sup>, and FF of 76.17%. Note that the performances of the other two ternary blend devices of **CH-6F** and **CH-6Cl** could be also improved (Table 3, Tables S13 and S15, ESI<sup>†</sup>), demonstrating that **F-2F** could help **CH**-series NFAs further improve the  $J_{SC}$  and  $V_{OC}$  with keeping high FF to achieve higher PCEs than the corresponding binary devices. Furthermore, the best **CH-4Cl**-based ternary devices were taken as an example to disclose enhanced light harvesting, improved exciton dissociation efficiency, charge transfer and charge collection efficiency, and optimized film morphology (see the figures and discussions in Fig. S23–S29, ESI<sup>†</sup>) after introducing **F-2F** as the third component. In addition, their effects on the CT states and non-radiative recombination losses will also be discussed below.

### Morphology analysis

To investigate the influence of peripheral halogenations on phase separation, we resorted to atomic force microscopy

(AFM) and transmission electron microscopy (TEM). As shown in the AFM images (Fig. 5a–f), all the blends exhibit a uniform and relatively smooth surface morphology, and the root-mean-square (RMS) surface roughness values for **PM6:CH-6F**, **PM6:CH-4Cl**, and **PM6:CH-6Cl** are 0.87, 0.93 and 1.01 nm, respectively. In addition, **CH-4Cl** and **CH-6Cl**-based blends present obvious fiber-like surface morphologies compared to that of **CH-6F**, which can be attributed to the stronger crystallization induced by chlorinated terminals. From the TEM image (Fig. S25, ESI<sup>†</sup>), **CH-4Cl** and **CH-6Cl**-based devices show slightly larger and more suitable phase separation, along with more obvious interpenetrated structures than that of **CH-6F**. The enhanced crystallization and superior interpenetrated networks for **CH-4Cl** and **CH-6Cl**-based blends are in good consistency with their improved electron mobility compared to that of the **CH-6F**-based one. In addition, after introducing **F-2F** as the third component, the **PM6:CH-4Cl:F-2F**-based film shows improved fiber-like surface morphologies (Fig. S23, ESI<sup>†</sup>) and an enlarged domain size (Fig. S25, ESI<sup>†</sup>), which partially account for its enhanced charge transport dynamics. These results suggest that the delicate tuning of peripheral halogenation in NFAs can achieve a suitable donor/acceptor distribution and phase separation scale in the blend films, leading to more efficient charge transport and enhanced  $J_{SC}$ . The contact angles of neat films were also measured (Fig. S29, Note S3, ESI<sup>†</sup>) and the corresponding miscibility parameters between donor and acceptor are summarized in Table S5 (ESI<sup>†</sup>). The reckoned Flory–Huggins interaction parameters  $\chi^{81,82}$  between **PM6** donor and **CH-6F**, **CH-4Cl**, **CH-6Cl**, and **Y6** acceptors are 0.31, 0.19, 0.34 and 0.40, respectively, suggesting that **PM6** and **CH-4Cl** show the suitable miscibility.

To further comprehend the impact of different molecular packing modes on the microstructures of neat and blend films based on these NFAs, grazing incidence wide-angle X-ray scattering (GIWAXS) was performed. As shown in Fig. S24 and Table S4 (ESI<sup>†</sup>), the neat **CH-6F**, **CH-4Cl**, **CH-6Cl** and **Y6** films exhibit a distinct  $\pi$ - $\pi$  stacking (010) peak at *ca.* 1.76, 1.79, 1.77 and 1.72 Å<sup>-1</sup> in the out-of-plane (OOP) direction with  $d_{\pi}$  ( $\pi$ - $\pi$  stacking distances) of *ca.* 3.56, 3.51, 3.54 and 3.65 Å, respectively, suggesting predominant face-on molecular packing patterns for all the NFAs. The smaller  $d_{\pi}$  of **CH**-series NFAs compared to that of **Y6** agrees well with the single crystal analysis (Table 2). More importantly, as displayed in Fig. S27

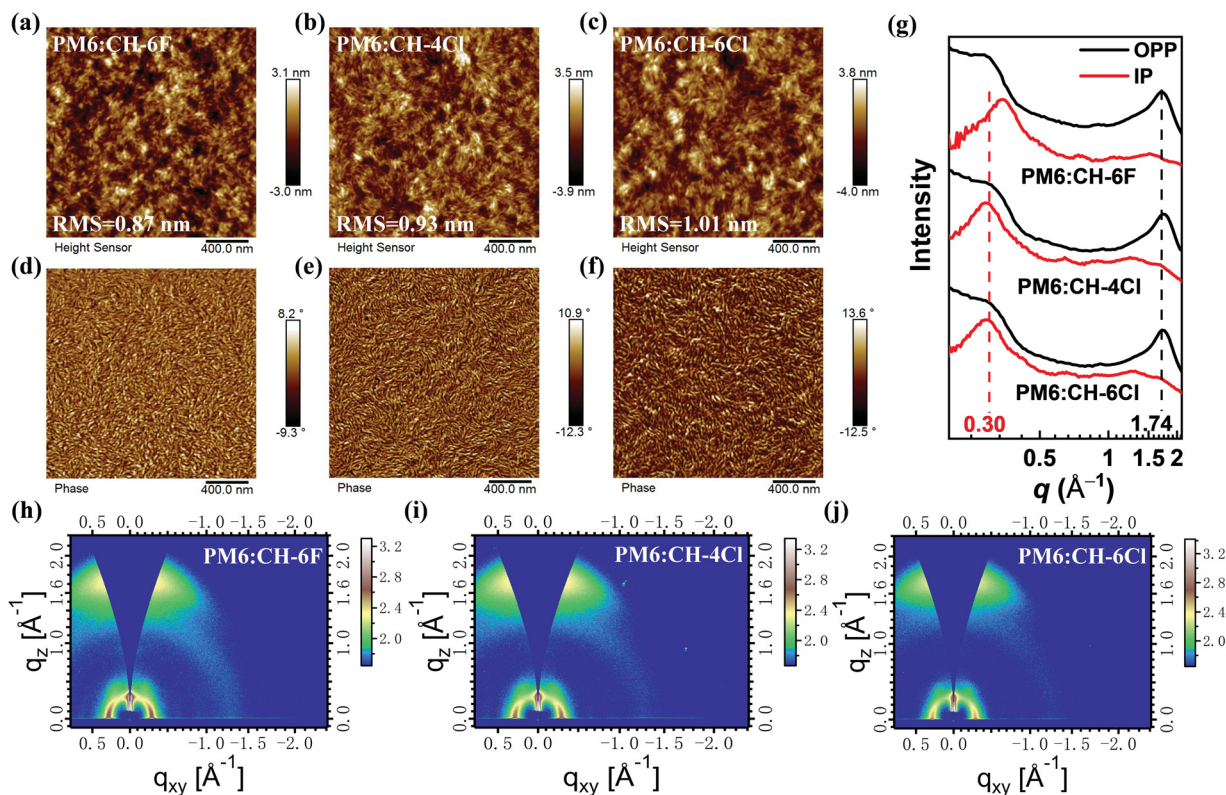


Fig. 5 Morphology characterization of blend films. (a–c) AFM height images. (d–f) AFM phase images. (g–i) 2D GIWAXS patterns and (j) 1D line-cuts of blend films of the **PM6:CH-6F**, **PM6:CH-4Cl**, and **PM6:CH-6Cl**-based devices.

(ESI<sup>†</sup>), there are strong peaks at 0.37, 0.49 and 1.81  $\text{\AA}^{-1}$  in the X-ray diffraction pattern generated from the single crystal structure of **CH-4Cl**, corresponding to the packing distances of 17.12, 12.33 and 3.44  $\text{\AA}$ , respectively. This matches well with the GIWAXS data in the **CH-4Cl** film, indicating that the packing modes of NFAs in single crystals can be largely preserved in the spin-coated films. Moreover, similar peaks can be also observed in both single crystals and spin-coated films for **CH-6F** and **CH-6Cl** (Fig. S26 and S28, ESI<sup>†</sup>).

The 2D GIWAXS images of the three blend films and the corresponding 1D line-cuts are presented in Fig. 5g–j and Table 4. All the blend films present face-on orientation indicated by the (100) diffraction peaks at *ca.* 0.30  $\text{\AA}^{-1}$  in the IP direction and (010) diffraction peaks at *ca.* 1.74  $\text{\AA}^{-1}$  in the OOP direction. In detail, the blend **CH-6F**, **CH-4Cl**, **CH-6Cl** and **Y6** films exhibit a distinct  $\pi$ - $\pi$  stacking (010) peak at *ca.* 1.74, 1.75, 1.74 and 1.71  $\text{\AA}^{-1}$  in the out-of-plane (OOP) direction with  $d_{\pi}$

( $\pi$ - $\pi$  stacking distances) of *ca.* 3.62, 3.58, 3.59 and 3.65  $\text{\AA}$ , respectively. **CH**-series based blend films exhibit smaller  $d_{\pi}$  compared with that of **Y6**, and **CH-4Cl** owns the smallest  $d_{\pi}$ , which agrees well with the single crystal analysis (Table 2). The corresponding crystal coherence lengths (CCLs) of (010)  $\pi$ - $\pi$  stacking peaks and (100) lamellar diffraction peaks are estimated to be 18.21 and 83.16  $\text{\AA}$  for **PM6:CH-6F**, 19.30 and 89.76  $\text{\AA}$  for **PM6:CH-4Cl**, 19.98 and 91.21  $\text{\AA}$  for **PM6:CH-6Cl** and 19.10 and 73.44  $\text{\AA}$  for **PM6:Y6**. The greatly enlarged CCLs for **PM6:CH-4Cl** and **PM6:CH-6Cl** compared to those of **PM6:CH-6F** and **PM6:Y6** should be caused by the increased crystallinity after peripheral chlorination, which agrees well with the data from AFM and TEM images. Moreover, the larger CCLs for **PM6:CH-4Cl** and **PM6:CH-6Cl** blends indicate the more ordered molecular packings and should result in lower energy disorder, which will be discussed in detail below. After adding **F-2F** as the third component, the **PM6:CH-4Cl:F-2F**

Table 4 The detailed parameters of the corresponding 2D GIWAXS

Materials	(010) peak				(100) peak			
	$q$ ( $\text{\AA}^{-1}$ )	$d$ -spacing <sup>a</sup> ( $\text{\AA}$ )	FWHM ( $\text{\AA}^{-1}$ )	CCL <sup>b</sup> ( $\text{\AA}$ )	$q$ ( $\text{\AA}^{-1}$ )	$d$ -spacing <sup>a</sup> ( $\text{\AA}$ )	FWHM ( $\text{\AA}^{-1}$ )	CCL <sup>b</sup> ( $\text{\AA}$ )
<b>PM6:CH-6F</b>	1.736	3.619	0.309	18.301	0.345	18.212	0.068	83.160
<b>PM6:CH-4Cl</b>	1.752	3.586	0.293	19.300	0.294	21.371	0.063	89.760
<b>PM6:CH-6Cl</b>	1.749	3.592	0.283	19.982	0.291	21.592	0.062	91.208

<sup>a</sup> Calculated from the equation:  $d$ -spacing =  $2\pi/q$ . <sup>b</sup> Obtained from the Scherrer equation:  $\text{CCL} = 2\pi K/\text{FWHM}$ , where FWHM is the full-width at half maximum and  $K$  is a shape factor ( $K = 0.9$  here).

blend demonstrates enhanced molecular packings in the interpenetrating networks with both smaller  $d_{\pi}$  of 3.56 Å and  $d_1$  of 21.16 Å relative to those of **CH-4Cl** based films, shown in Table S4 (ESI†). To sum up, precisely chosen peripheral halogenation can effectively adjust the crystallization of NFAs, control face-on orientation and then control molecular stacking of the corresponding blend films, leading to higher  $J_{SC}$  and FF values in the corresponding OSCs.

### Energy loss analysis of OSCs

Minimizing energy loss ( $E_{loss}$ ) to maximize  $V_{OC}$  and further improve the PCEs has been regarded as one of the most crucial issues in OSCs.<sup>32,83</sup> The  $E_{loss}$  of OSCs is closely related to the molecular packing of light harvesting components; therefore, the energy loss analysis has been conducted to disclose the effects of different peripheral halogenations. The total  $E_{loss}$  of OSCs can be determined by the following equation:  $E_{loss} = E_g - eV_{OC}$ , where  $E_g$  is estimated by the cross-point of normalized absorption and emission spectra of neat film,<sup>84,85</sup> being 1.381, 1.429, 1.409, and 1.400 eV for **Y6**, **CH-6F**, **CH-4Cl** and **CH-6Cl**, respectively (Fig. S30, ESI†), and the tendency of gradually narrowing bandgaps for **CH-series** NFAs agree well with those of  $E_g^{opt}$ , shown in Table 1. As a result, the total  $E_{loss}$  values of **Y6**-, **CH-6F**-, **CH-4Cl**- and **CH-6Cl**-based OSCs can be estimated to be 0.529, 0.557, 0.537 and 0.533 eV, respectively. In detail, the  $E_{loss}$  values of OSCs should originate from three parts:  $\Delta E_{CT}$ ,  $q\Delta V_r$  and  $q\Delta V_{nr}$ .<sup>83</sup> Among them,  $\Delta E_{CT}$  is the energetic difference between the local exciton (LE) state and charge transfer (CT) state.  $q\Delta V_r$  represents the energy loss induced by inevitable radiative recombination and is hard to be depressed.<sup>86</sup>

$q\Delta V_{nr}$  is the energy loss caused by the most-concerned non-radiative recombination and the suppression of  $q\Delta V_{nr}$  through molecular systematic engineering has been regarded as the most approached but challenging issue to further improve the  $V_{OC}$  and even PCEs of OSCs.<sup>87</sup>

Note that the absorption of CT states contributes to the low energy part of EQE spectra, thus the  $E_{CT}$  of OSCs can be estimated by fitting the highly sensitive EQEs (sEQE) and electroluminescence (EL) spectra (Fig. 6a–c, Fig. S32, S33 and S34, ESI†).<sup>83</sup> Consequently, the  $E_{CT}$  values of OSCs based on **PM6:Y6**, **PM6:CH-6F**, **PM6:CH-4Cl** and **PM6:CH-6Cl** are determined to be 1.328, 1.363, 1.369 and 1.367 eV, leading to the  $\Delta E_{CT}$  values of 0.066, 0.040, 0.033 and 0.053 eV, respectively (Table 5). With such a high CT state close to its LE state, the potential hybridization of LE and CT states caused by electronic couplings ( $t_{LE-CT}$ ) should be taken into consideration based on the recently developed three-state model (Fig. 6d).<sup>88,89</sup> There are no clear sub-bandgap CT-state features from both sEQE and EL measurements of these OSCs,<sup>58</sup> also implying the occurrence of hybridization of the LE and CT states in these blends with their small  $\Delta E_{CT}$ . The reduced  $\Delta E_{CT}$  of **CH-4Cl** and **CH-6Cl** blends compared with those of **CH-6F** and **Y6** (Table 5) could render more sufficient hybridization of the CT state with the LE state and the weakened electron-vibration coupling between the lowest energy CT state and the highest vibrational ground (G) state,<sup>71,90</sup> thus enlarging the radiative rate of the CT state *via* an intensity borrowing mechanism or the energetically possible back transition from the CT state to the LE state.<sup>89</sup> These characteristics can depress the non-radiative recombination and contribute to stronger emission of **CH-4Cl** and **CH-6Cl**

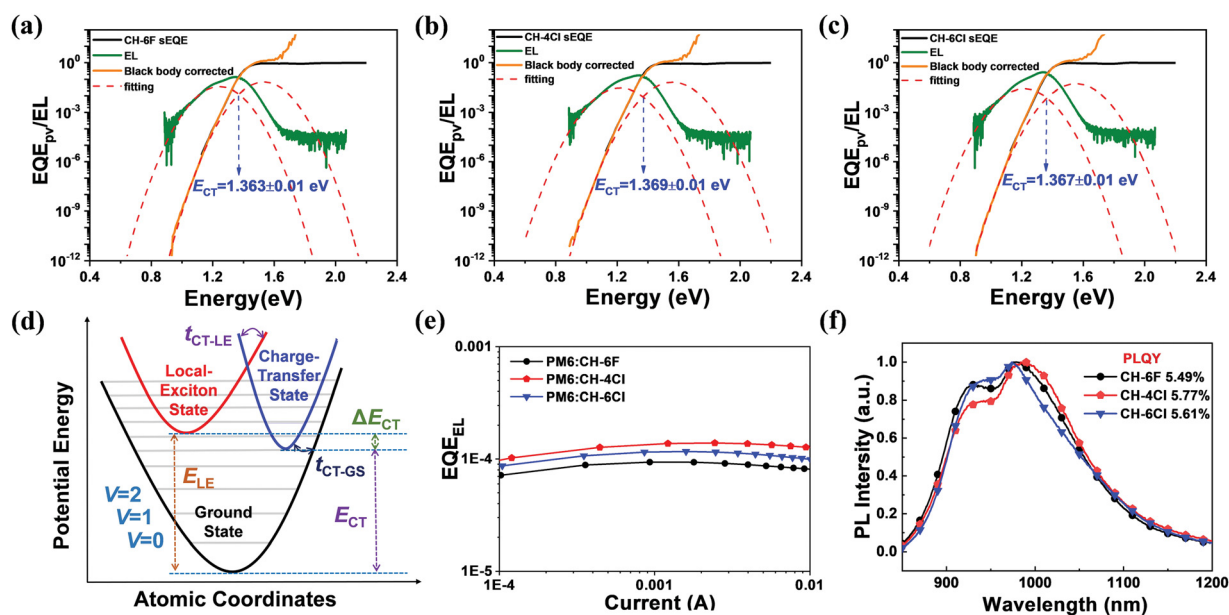


Fig. 6 Energy loss analysis. (a–c) Sensitive external quantum efficiency (sEQE) spectra and the fitting results for the relevant devices (Note S4, ESI†). (d) A schematic diagram of the potential energy curves for the ground (G), charge transfer (CT) and local exciton (LE) diatomic states;  $\Delta E_{CT}$  denotes the relaxed excitation energy of the LE and CT states, whereas  $t_{CT-G}$  and  $t_{LE-CT}$  represent the electronic couplings of the CT state with the G and LE states, respectively. (e) EQE<sub>EL</sub> spectra of the **PM6:CH-6F**, **PM6:CH-4Cl** and **PM6:CH-6Cl** based OSCs. (f) Photoluminescence spectra of these films excited at 826 nm together with their quantum efficiencies. Photoluminescence curves and fluorescence quenching efficiencies are shown in Fig. S31, ESI.†

Table 5 Detailed energy losses of the OSCs based on the studied NFAs

Active layer	$V_{OC}$ (V)	$E_g^a$ (eV)	$E_{CT}^b$ (eV)	$\Delta E_{CT}^c$ (eV)	$\Delta V_r^d$ (V)	$\Delta V_{nr}^e$ (V)	$E_{loss}$ (eV)	$EQE_{EL}$	$E_u^f$ (V)
<b>PM6:Y6</b>	0.852	1.381	1.328 ± 0.01	0.053	0.231	0.243	0.529	5.98 × 10 <sup>-5</sup>	24.70
<b>PM6:CH-6F</b>	0.872	1.429	1.363 ± 0.01	0.066	0.259	0.232	0.557	9.37 × 10 <sup>-5</sup>	23.30
<b>PM6:CH-4Cl</b>	0.872	1.409	1.369 ± 0.01	0.040	0.273	0.224	0.537	1.56 × 10 <sup>-4</sup>	21.98
<b>PM6:CH-6Cl</b>	0.867	1.400	1.367 ± 0.01	0.033	0.269	0.231	0.533	1.15 × 10 <sup>-4</sup>	22.11
<b>PM6:CH-4Cl:F-2F</b>	0.896	1.409	1.371 ± 0.01	0.038	0.271	0.203	0.513	2.92 × 10 <sup>-4</sup>	22.08

<sup>a</sup> Band gap estimated *via* the intersection of normalized absorption and PL spectra. <sup>b</sup>  $E_{CT}$  was obtained by fittings (dashed curve in Fig. 6 and Fig. S30–S37, ESI). <sup>c</sup>  $\Delta E_{CT}$  was calculated by following the equation:  $\Delta E_{CT} = E_g - E_{CT}$ . <sup>d</sup>  $\Delta V_r$  was calculated by following the equation:  $\Delta V_r = E_{CT} / q - \Delta V_{OC} - \Delta V_{nr}$ . <sup>e</sup>  $\Delta V_{nr}$  was calculated by following the equation:  $\Delta V_{nr} = (kT/q) \ln(1/EQE_{EL})$ . <sup>f</sup> Urbach energies.

blends. This is consistent with their smaller  $\Delta V_{nr}$  of 0.224 V and 0.231 V with respect to that of 0.243 and 0.232 V for **Y6** and **CH-6F**, respectively, which can be indicated by the higher  $EQE_{EL}$  in Fig. 6e and Fig. S35 (ESI<sup>†</sup>). Given that the limit of  $\Delta V_{nr}$  in organic solar cells could be defined by the PLQY of pristine material components when  $\Delta E_{CT}$  is small,<sup>88,89</sup> the smaller  $\Delta V_{nr}$  values of **CH-4Cl** and **CH-6Cl** are also consistent with their higher photoluminescence quantum yield (PLQY) of 5.77% and 5.61% compared to that of 5.49% for **CH-6F** and 4.80% for **Y6** in the pristine material as shown in Fig. 6f and Fig. S36 (ESI<sup>†</sup>). The reduced  $\Delta V_{nr}$  of **CH-4Cl** and **CH-6Cl**-based OSCs should account for their comparable  $V_{OC}$  with that of **CH-6F**, which should be caused by their optimized interpenetrating network and strong packing modes based on our single crystal analysis above.

Moreover, we also analyzed the Urbach energies ( $E_u$ ) in the active layers, which is determined by the width of the tail of the electronic density of states (DOS) for photoactive layers<sup>91</sup> and reflects the degree of overall energy disorder.<sup>92</sup> By fitting the sEQE onset (Fig. S32 and S37, ESI<sup>†</sup>), **CH-4Cl**- and **CH-6Cl**-based OSCs show the comparable  $E_u$  values of 21.98 and 22.11 meV, respectively, smaller than 23.30 meV for **CH-6F**- and 24.70 meV for **Y6**-based devices (Table 5). In general, smaller  $E_u$  values for **CH-4Cl** and **CH-6Cl** are indicative of a lower static disorder and hence account for their reduced charge recombination.<sup>93</sup> Note that the smaller  $E_u$  for **CH-4Cl** and **CH-6Cl** could be attributed to their more ordered molecular packings caused by the simplified but superior packing modes. In addition, compared to the corresponding binary devices, the **PM6:CH-4Cl:F-2F** ternary device exhibits a higher  $E_{CT}$  value of 1.371 eV, a reduced  $\Delta E_{CT}$  of 0.038 eV, a similar  $E_u$  value of 22.08 meV, and thus a smaller  $\Delta V_{nr}$  of ~0.203 V (Table 5 and Fig. S30–S37, ESI<sup>†</sup>). Moreover, the total  $E_{loss}$  of the **PM6:CH-4Cl:F-2F**-based device is 0.513 eV, ranking **CH-4Cl** based OSCs among the smallest  $E_{loss}$  systems.

To summarize, based on all the above molecular structure and morphology analyses of single crystals, GIWAXS, AFM, TEM *etc.* for **CH**-series NFAs and the photodynamic and performance of resulting OSCs, some important conclusions related to the important role of peripheral halogenation could be noted: (I) at the molecular level, peripheral halogenation could not only tune the energy levels delicately but also affect the molecular rigidity and planarity which could contribute to a reduced reorganization energy; (II) in the solid states, such a little modification of peripheral halogens in NFAs leads to

diverse intermolecular packing modes and completely changed molecular networks, which have a dramatical influence on the micromorphology of the blend films, charge transfer/transport dynamics and also energetic disorder; (III) when coming to the device level, the different peripheral halogenations on NFAs could affect the feature of the CT states, tune the degree of the hybridization between the CT and LE states, and thus suppress the non-radiative recombination process and improve the photovoltaic performance of OSCs; and (IV) all the results above have proven that peripheral halogenation engineering is an effective strategy to further boost the PCEs of high-performance OSCs through delicate molecular stacking control.

## Conclusions

To conclude, a series of A–D–A type **CH**-series NFAs have been designed and synthesized, featuring multiple peripheral halogenations in both conjugated extended central units and end groups, to unveil the effects of different peripheral halogenations on the optoelectronic properties, molecular stackings, and even PCEs of OSCs systematically. Crystallographic analysis indicates that peripheral halogenation with different halogens leads to dramatically different single crystal structures and packing modes. Among them, **CH-4Cl** and **CH-6Cl** demonstrate several unobserved packing modes of “dual E/C”, “dual C/b” and “E/C” in the state-of-the-art **Y**-series NFAs. Compared with **CH-6F** and **Y6**, **CH-4Cl** and **CH-6Cl** possess greatly reduced electron reorganization energies and shorter intermolecular packing distances, and exhibit more balanced charge mobilities, better phase separation, and lower energy disorder when blended with **PM6** donor. In addition, the reduced energy offset between the CT and LE states of **CH-4Cl** and **CH-6Cl** may result in the enhanced hybridization of the CT and LE states and thus suppress the non-radiative recombination losses. Finally, high-efficient OSCs have been afforded for all these three compound devices, especially with a champion PCE of 18.22% and a markedly reduced  $\Delta V_{nr}$  of 0.203 V by utilizing **CH-4Cl** NFA for its ternary device. These results reveal that the molecular packing modes, charge transfer/transport properties, and even PCEs of OSCs could be optimized by a simple modification of peripheral halogens in NFAs with exactly the same backbone structure and will stimulate the further exploration of peripheral halogenation engineering with the aim of boosting PCEs especially in high-performance OSCs.

## Data availability

Data supporting the findings of this study are available within the paper and its ESI†. Source data are provided in this paper. The X-ray crystallographic coordinates for structures of **CH-6F**, **CH-4Cl** and **CH-6Cl** have been deposited at the Cambridge Crystallographic Data Centre (CCDC) with 2168458, 2168455 and 2168457†.

## Author contributions

The synthetic works were carried out by H. C., and Y. Z. carried out the device fabrication and measurements. G. L., M. L. and H. Z. carried out the theoretical computation of **CH-6F**, **CH-4Cl** and **CH-6Cl** acceptors. H. C. synthesised these acceptors. Y. Z. grew the related single crystals. Y. Z. and G. L. solved and analyzed the single-crystal structures of these acceptors. X. X. and Z. M. performed the EL, EQE<sub>EL</sub> and sEQE experiments and analyzed the data. Y. Z. performed the space-charge-limited current measurements and performed the morphology characterization and analyzed the data. C. L. and X. W. helped to analyze the data and revise the manuscript. Z. Y., X. W. and Y. C. supervised and directed this project. All authors discussed the results and commented on the manuscript.

## Conflicts of interest

The authors declare no competing interests.

## Acknowledgements

The authors gratefully acknowledge the financial support from NSFC (21935007, 52025033, 51873089) and MoST (2019YF-A0705900) of China, Tianjin city (20JCZDJC00740), 111 Project (B12015) and the 100 Young Academic Leaders Program of Nankai University (No. 020-ZB22000110 and 020-92220002). The authors also gratefully acknowledge the support from Dr Xiaohu Miao for single crystal characterization in the Instrumentation and Service Center for Physical Sciences, Westlake University and Prof. Zhixiang Wei from National Center for Nanoscience and Technology of China provided GIWAXS measurements.

## References

- 1 A. Polman, M. Knight, E. C. Garnett, B. Ehrler and W. C. Sinke, *Science*, 2016, **352**, aad4424.
- 2 J. Zhang, H. S. Tan, X. Guo, A. Facchetti and H. Yan, *Nat. Energy*, 2018, **3**, 720–731.
- 3 H.-H. Gao, Y. Sun, Y. Cai, X. Wan, L. Meng, X. Ke, S. Li, Y. Zhang, R. Xia, N. Zheng, M. Zhang, H.-L. Yip, Y. Cao and Y. Chen, *Adv. Energy Mater.*, 2019, **9**, 1901024.
- 4 X. Guo, Q. Fan, J. Wu, G. Li, Z. Peng, W. Su, J. Lin, L. Hou, Y. Qin, H. Ade, L. Ye, M. Zhang and Y. Li, *Angew. Chem., Int. Ed.*, 2021, **133**, 2352–2359.
- 5 Q. Fan, Y. Wang, M. Zhang, B. Wu, X. Guo, Y. Jiang, W. Li, B. Guo, C. Ye, W. Su, J. Fang, X. Ou, F. Liu, Z. Wei, T. C. Sum and T. P. Russell, *Adv. Mater.*, 2018, **30**, 1704546.
- 6 D. Hu, Q. Yang, H. Chen, F. Wobben, V. M. Le Corre, R. Singh, T. Liu, R. Ma, H. Tang, L. J. A. Koster, T. Duan, H. Yan, Z. Kan, Z. Xiao and S. Lu, *Energy Environ. Sci.*, 2020, **13**, 2134–2141.
- 7 G. Li, R. Zhu and Y. Yang, *Nat. Photonics*, 2012, **6**, 153–161.
- 8 G. Dennler, M. C. Scharber and C. J. Brabec, *Adv. Mater.*, 2009, **21**, 1323–1338.
- 9 L. Meng, Y. Zhang, X. Wan, C. Li, X. Zhang, Y. Wang, X. Ke, Z. Xiao, L. Ding, R. Xia, H.-L. Yip, Y. Cao and Y. Chen, *Science*, 2018, **361**, 1094–1098.
- 10 M. Zhang, L. Zhu, G. Zhou, T. Hao, C. Qiu, Z. Zhao, Q. Hu, B. W. Larson, H. Zhu, Z. Ma, Z. Tang, W. Feng, Y. Zhang, T. P. Russell and F. Liu, *Nat. Commun.*, 2021, **12**, 1–10.
- 11 C. Li, J. Zhou, J. Song, J. Xu, H. Zhang, X. Zhang, J. Guo, L. Zhu, D. Wei, G. Han, J. Min, Y. Zhang, Z. Xie, Y. Yi, H. Yan, F. Gao, F. Liu and Y. Sun, *Nat. Energy*, 2021, **6**, 605–613.
- 12 Z. Zheng, J. Wang, P. Bi, J. Ren, Y. Wang, Y. Yang, X. Liu, S. Zhang and J. Hou, *Joule*, 2021, **6**, 171–184.
- 13 Y. Cui, Y. Xu, H. Yao, P. Bi, L. Hong, J. Zhang, Y. Zu, T. Zhang, J. Qin, J. Ren, Z. Chen, C. He, X. Hao, Z. Wei and J. Hou, *Adv. Mater.*, 2021, **33**, 2102420.
- 14 Q. Liu, Y. Jiang, K. Jin, J. Qin, J. Xu, W. Li, J. Xiong, J. Liu, Z. Xiao, K. Sun, S. Yang, X. Zhang and L. Ding, *Sci. Bull.*, 2020, **65**, 272–275.
- 15 X. Meng, K. Jin, Z. Xiao and L. Ding, *J. Semicond.*, 2021, **42**, 100501.
- 16 C. He, Y. Pan, Y. Ouyang, Q. Shen, Y. Gao, K. Yan, J. Fang, Y. Chen, C. Ma, J. Min, C. Zhang, L. Zuo and H. Chen, *Energy Environ. Sci.*, 2022, **15**, 2537–2544.
- 17 R. Sun, Y. Wu, X. Yang, Y. Gao, Z. Chen, K. Li, J. Qiao, T. Wang, J. Guo, C. Liu, X. Hao, H. Zhu and J. Mie, *Adv. Mater.*, 2022, **34**, 2110147.
- 18 L. Zhu, M. Zhang, J. Xu, C. Li, J. Yan, G. Zhou, W. Zhong, T. Hao, J. Song, X. Xue, Z. Zhou, R. Zeng, H. Zhu, C.-C. Chen, R. C. I. MacKenzie, Y. Zou, J. Nelson, Y. Zhang, Y. Sun and F. Liu, *Nat. Mater.*, 2022, **21**, 656–663.
- 19 Z. Bi, K. Chen, L. Gou, Y. Guo, X. Zhou, H. B. Naveed, J. Wang, Q. Zhu, J. Yuan, C. Zhao, K. Zhou, S. Chandrabose, Z. Tang, Y. Yi, J. M. Hodgkiss, L. Zhang and W. Ma, *J. Mater. Chem. A*, 2021, **9**, 16733–16742.
- 20 G. Zhang, J. Zhao, P. C. Chow, K. Jiang, J. Zhang, Z. Zhu, J. Zhang, F. Huang and H. Yan, *Chem. Rev.*, 2018, **118**, 3447–3507.
- 21 C. Yan, S. Barlow, Z. Wang, H. Yan, A. K.-Y. Jen, S. R. Marder and X. Zhan, *Nat. Rev. Mater.*, 2018, **3**, 1–19.
- 22 D. Li, X. Zhang, D. Liu and T. Wang, *J. Mater. Chem. A*, 2020, **8**, 15607–15619.
- 23 G. Han and Y. Yi, *Acc. Chem. Res.*, 2022, **55**, 2585–2591.
- 24 Y. Li, Y. Guo, Z. Chen, L. Zhan, C. He, Z. Bi, N. Yao, S. Li, G. Zhou, Y. Yi, Y. Yang, H. Zhu, W. Ma, F. Gao, F. Zhang, L. Zuo and H. Chen, *Energy Environ. Sci.*, 2022, **15**, 855–865.
- 25 W. Zhao, D. Qian, S. Zhang, S. Li, O. Inganäs, F. Gao and J. Hou, *Adv. Mater.*, 2016, **28**, 4734–4739.

- 26 B. Kan, Y. Kan, L. Zuo, X. Shi and K. Gao, *InfoMat*, 2021, **3**, 175–200.
- 27 H.-H. Gao, Y. Sun, X. Wan, X. Ke, H. Feng, B. Kan, Y. Wang, Y. Zhang, C. Li and Y. Chen, *Adv. Sci.*, 2018, **5**, 1800307.
- 28 D. Meng, R. Zheng, Y. Zhao, E. Zhang, L. Dou and Y. Yang, *Adv. Mater.*, 2022, **34**, 2107330.
- 29 C. Duan and L. Ding, *Sci. Bull.*, 2020, **65**, 1231–1233.
- 30 W. Zhu, J. M. Alzola, T. J. Aldrich, K. L. Kohlstedt, D. Zheng, P. E. Hartnett, N. D. Eastham, W. Huang, G. Wang, R. M. Young, G. C. Schatz, M. R. Wasielewski and A. Facchetti, *ACS Energy Lett.*, 2019, **4**, 2695–2702.
- 31 Y. Sun, H.-H. Gao, Y.-Q.-Q. Yi, X. Wan, H. Feng, X. Ke, Y. Zhang, J. Yan, C. Li and Y. Chen, *Sci. China Mater.*, 2019, **62**, 1210–1217.
- 32 Y. Cui, H. Yao, J. Zhang, T. Zhang, Y. Wang, L. Hong, K. Xian, B. Xu, S. Zhang, J. Peng, Z. Wei, F. Gao and J. Hou, *Nat. Commun.*, 2019, **10**, 1–8.
- 33 A. Ashokan, T. Wang, M. K. Ravva and J.-L. Brédas, *J. Mater. Chem. C*, 2018, **6**, 13162–13170.
- 34 L. Benatto and M. Koehler, *J. Phys. Chem. C*, 2019, **123**, 6395–6406.
- 35 R. Ma, G. Li, D. Li, T. Liu, Z. Luo, G. Zhang, M. Zhang, Z. Wang, S. Luo, T. Yang, F. Liu, H. Yan and B. Tang, *Sol. RRL*, 2020, **4**, 2000250.
- 36 P. Chao, H. Chen, M. Pu, Y. Zhu, L. Han, N. Zheng, J. Zhou, X. Chang, D. Mo, Z. Xie, H. Meng and F. He, *Adv. Sci.*, 2021, **8**, 2003641.
- 37 Q. Liao, Q. Kang, Y. Yang, C. An, B. Xu and J. Hou, *Adv. Mater.*, 2020, **32**, 1906557.
- 38 Q. He, M. Shahid, X. Jiao, E. Gann, F. D. Eisner, T. Wu, Z. Fei, T. D. Anthopoulos, C. R. McNeill and M. Heeney, *ACS Appl. Mater. Interfaces*, 2020, **12**, 9555–9562.
- 39 Y. Chen, R. Ma, T. Liu, Y. Xiao, H. K. Kim, J. Zhang, C. Ma, H. Sun, F. Bai, X. Guo, K. S. Wong, X. Lu and H. Yan, *Adv. Energy Mater.*, 2021, **11**, 2003777.
- 40 Q. Zhang, M. A. Kelly, N. Bauer and W. You, *Acc. Chem. Res.*, 2017, **50**, 2401–2409.
- 41 X. Zhang, G. Li, S. Mukherjee, W. Huang, D. Zheng, L. W. Feng, Y. Chen, J. Wu, V. K. Sangwan, M. C. Hersam, D. M. DeLongchamp, J. Yu, A. Facchetti and T. J. Marks, *Adv. Energy Mater.*, 2022, **12**, 2102172.
- 42 Q. Zhang, X. Song, R. Singh, S. Chung, Z. Zhou, Y. Lu, B. Zhang, K. Cho, W. Zhu and Y. Liu, *Chem. Eng. J.*, 2022, **437**, 135182.
- 43 H. Yu, Z. Qi, J. Yu, Y. Xiao, R. Sun, Z. Luo, A. M. H. Cheung, J. Zhang, H. Sun, W. Zhou, S. Chen, X. Guo, X. Lu, F. Gao, J. Min and H. Yan, *Adv. Energy Mater.*, 2021, **11**, 2003171.
- 44 M. Nam, M. Cha, H. H. Lee, K. Hur, K.-T. Lee, J. Yoo, I. K. Han, S. J. Kwon and D.-H. Ko, *Nat. Commun.*, 2017, **8**, 1–10.
- 45 S. Lu, F. Li, K. Zhang, J. Zhu, W. Cui, R. Yang, L. Yu and M. Sun, *Sol. Energy*, 2020, **195**, 429–435.
- 46 Y. Cui, H. Yao, L. Hong, T. Zhang, Y. Tang, B. Lin, K. Xian, B. Gao, C. An, P. Bi, W. Ma and J. Hou, *Natl. Sci. Rev.*, 2020, **7**, 1239–1246.
- 47 Q. Wang, M. Li, X. Zhang, Y. Qin, J. Wang, J. Zhang, J. Hou, R. A. Janssen and Y. Geng, *Macromolecules*, 2019, **52**, 4464–4474.
- 48 Q. Zhang, L. Yan, X. Jiao, Z. Peng, S. Liu, J. J. Rech, E. Klump, H. Ade, F. So and W. You, *Chem. Mater.*, 2017, **29**, 5990–6002.
- 49 C. Duan, G. Zango, M. García Iglesias, F. J. Colberts, M. M. Wienk, M. V. Martínez-Díaz, R. A. Janssen and T. Torres, *Angew. Chem., Int. Ed.*, 2017, **129**, 154–158.
- 50 H. Ji, J. Li, M. Du, J. Yang, A. Tang, G. Li, Q. Guo and E. Zhou, *J. Phys. Chem. C*, 2021, **125**, 10876–10882.
- 51 Y. Lin, J. Wang, Z. G. Zhang, H. Bai, Y. Li, D. Zhu and X. Zhan, *Adv. Mater.*, 2015, **27**, 1170–1174.
- 52 H. Yao, Y. Cui, R. Yu, B. Gao, H. Zhang and J. Hou, *Angew. Chem., Int. Ed.*, 2017, **129**, 3091–3095.
- 53 X. Ke, L. Meng, X. Wan, M. Li, Y. Sun, Z. Guo, S. Wu, H. Zhang, C. Li and Y. Chen, *J. Mater. Chem. A*, 2020, **8**, 9726–9732.
- 54 N. Qiu, H. Zhang, X. Wan, C. Li, X. Ke, H. Feng, B. Kan, H. Zhang, Q. Zhang, Y. Lu and Y. Chen, *Adv. Mater.*, 2017, **29**, 1604964.
- 55 W. Zhao, S. Li, H. Yao, S. Zhang, Y. Zhang, B. Yang and J. Hou, *J. Am. Chem. Soc.*, 2017, **139**, 7148–7151.
- 56 Y. Wang, Y. Zhang, N. Qiu, H. Feng, H. Gao, B. Kan, Y. Ma, C. Li, X. Wan and Y. Chen, *Adv. Energy Mater.*, 2018, **8**, 1702870.
- 57 W. Zhu, A. P. Spencer, S. Mukherjee, J. M. Alzola, V. K. Sangwan, S. H. Amsterdam, S. M. Swick, L. O. Jones, M. C. Heiber, A. A. Herzing, G. Li, C. L. Stern, D. M. DeLongchamp, K. L. Kohlstedt, M. C. Hersam, G. C. Schatz, M. R. Wasielewski, L. X. Chen, A. Facchetti and T. J. Marks, *J. Am. Chem. Soc.*, 2020, **142**, 14532–14547.
- 58 G. Zhang, X.-K. Chen, J. Xiao, P. C. Chow, M. Ren, G. Kupgan, X. Jiao, C. Chan, X. Du, R. Xia, Z. Chen, J. Yuan, Y. Zhang, S. Zhang, Y. Liu, Y. Zou, H. Yan, K. S. Wong, V. Coropceanu, N. Li, C. J. Brabec, J.-L. Bredas, H.-L. Yip and Y. Cao, *Nat. Commun.*, 2020, **11**, 1–10.
- 59 J. Cao, L. Yi and L. Ding, *J. Semicond.*, 2022, **43**, 030202.
- 60 H. Chen, H. Lai, Z. Chen, Y. Zhu, H. Wang, L. Han, Y. Zhang and F. He, *Angew. Chem., Int. Ed.*, 2021, **60**, 3238–3246.
- 61 F. Qi, L. O. Jones, K. Jiang, S.-H. Jang, W. Kaminsky, J. Oh, H. Zhang, Z. Cai, C. Yang, K. L. Kohlstedt, G. C. Schatz, F. R. Lin, T. J. Marks and A. K.-Y. Jen, *Mater. Horiz.*, 2022, **9**, 403–410.
- 62 Z. Zhou, W. Liu, G. Zhou, M. Zhang, D. Qian, J. Zhang, S. Chen, S. Xu, C. Yang, F. Gao, H. Zhu, F. Liu and X. Zhu, *Adv. Mater.*, 2020, **32**, 1906324.
- 63 C. Zhu, K. An, W. Zhong, Z. Li, Y. Qian, X. Su and L. Ying, *Chem. Commun.*, 2020, **56**, 4700–4703.
- 64 H. Chen, Y. Zou, H. Liang, T. He, X. Xu, Y. Zhang, Z. Ma, J. Wang, M. Zhang, Q. Li, C. Li, G. Long, X. Wan, Z. Yao and Y. Chen, *Sci. China Chem.*, 2022, **65**, 1362–1373.
- 65 G. Li, X. Zhang, L. O. Jones, J. M. Alzola, S. Mukherjee, L.-W. Feng, W. Zhu, C. L. Stern, W. Huang, J. Yu, V. K. Sangwan, D. M. DeLongchamp, K. L. Kohlstedt, M. R. Wasielewski, M. C. Hersam, G. C. Schatz, A. Facchetti and T. J. Marks, *J. Am. Chem. Soc.*, 2021, **143**, 6123–6139.
- 66 X. Wan, C. Li, M. Zhang and Y. Chen, *Chem. Soc. Rev.*, 2020, **49**, 2828–2842.
- 67 P. Politzer and J. S. Murray, *Struct. Chem.*, 2021, **32**, 623–629.

- 68 Z. Shuai, H. Geng, W. Xu, Y. Liao and J.-M. André, *Chem. Soc. Rev.*, 2014, **43**, 2662–2679.
- 69 R. A. Marcus, *Rev. Mod. Phys.*, 1993, **65**, 599.
- 70 H. Geng, Q. Peng, L. Wang, H. Li, Y. Liao, Z. Ma and Z. Shuai, *Adv. Mater.*, 2012, **24**, 3568–3572.
- 71 D. Qian, Z. Zheng, H. Yao, W. Tress, T. R. Hopper, S. Chen, S. Li, J. Liu, S. Chen, J. Zhang, X.-K. Liu, B. Gao, L. Ouyang, Y. Jin, G. Pozina, I. A. Buyanova, W. M. Chen, O. Inganäs, V. Coropceanu, J.-L. Bredas, H. Yan, J. Hou, F. Zhang, A. A. Bakulin and F. Gao, *Nat. Mater.*, 2018, **17**, 703–709.
- 72 Q. Liu, Y. Jiang, K. Jin, J. Qin, J. Xu, W. Li, J. Xiong, J. Liu, Z. Xiao, K. Sun, S. Yang, X. Zhang and L. Ding, *Sci. Bull.*, 2020, **65**, 272–275.
- 73 K. Chong, X. Xu, H. Meng, J. Xue, L. Yu, W. Ma and Q. Peng, *Adv. Mater.*, 2022, **34**, 2109516.
- 74 F. Liu, L. Zhou, W. Liu, Z. Zhou, Q. Yue, W. Zheng, R. Sun, W. Liu, S. Xu, H. Fan, L. Feng, Y. Yi, W. Zhang and X. Zhu, *Adv. Mater.*, 2021, **33**, 2100830.
- 75 L. Zhan, S. Li, T.-K. Lau, Y. Cui, X. Lu, M. Shi, C.-Z. Li, H. Li, J. Hou and H. Chen, *Energy Environ. Sci.*, 2020, **13**, 635–645.
- 76 S. Li, L. Zhan, Y. Jin, G. Zhou, T. K. Lau, R. Qin, M. Shi, C. Z. Li, H. Zhu, X. Lu, F. Zhang and H. Chen, *Adv. Mater.*, 2020, **32**, 2001160.
- 77 Q. Ma, Z. Jia, L. Meng, J. Zhang, H. Zhang, W. Huang, J. Yuan, F. Gao, Y. Wan, Z. Zhang and Y. Li, *Nano Energy*, 2020, **78**, 105272.
- 78 T. Liu, R. Ma, Z. Luo, Y. Guo, G. Zhang, Y. Xiao, T. Yang, Y. Chen, G. Li, Y. Yi, X. Lu, H. Yan and B. Tang, *Energy Environ. Sci.*, 2020, **13**, 2115–2123.
- 79 Q. An, J. Wang, X. Ma, J. Gao, Z. Hu, B. Liu, H. Sun, X. Guo, X. Zhang and F. Zhang, *Energy Environ. Sci.*, 2020, **13**, 5039–5047.
- 80 R. Ma, C. Yan, P. W. K. Fong, J. Yu, H. Liu, J. Yin, J. Huang, X. Lu, H. Yan and G. Li, *Energy Environ. Sci.*, 2022, **15**, 2479–2488.
- 81 S. Nilsson, A. Bernasik, A. Budkowski and E. Moons, *Macromolecules*, 2007, **40**, 8291–8301.
- 82 S. Honda, H. Ohkita, H. Benten and S. Ito, *Adv. Energy Mater.*, 2011, **1**, 588–598.
- 83 H. Liu, M. Li, H. Wu, J. Wang, Z. Ma and Z. Tang, *J. Mater. Chem. A*, 2021, **9**, 19770–19777.
- 84 Y. Wang, D. Qian, Y. Cui, H. Zhang, J. Hou, K. Vandewal, T. Kirchartz and F. Gao, *Adv. Energy Mater.*, 2018, **8**, 1801352.
- 85 K. Vandewal, J. Benduhn and V. Nikolis, *Sustainable Energy Fuels*, 2018, **2**, 538–544.
- 86 O. D. Miller, E. Yablonovitch and S. R. Kurtz, *IEEE J. Photovolt.*, 2012, **2**, 303–311.
- 87 N. An, Y. Cai, H. Wu, A. Tang, K. Zhang, X. Hao, Z. Ma, Q. Guo, H. S. Ryu, H. Y. Woo, Y. Sun and E. Zhou, *Adv. Mater.*, 2020, **32**, 2002122.
- 88 X.-K. Chen, D. Qian, Y. Wang, T. Kirchartz, W. Tress, H. Yao, J. Yuan, M. Hülsbeck, M. Zhang, Y. Zou, Y. Sun, Y. Li, J. Hou, O. Inganäs, V. Coropceanu, J.-L. Bredas and G. Feng, *Nat. Energy*, 2021, **6**, 799–806.
- 89 F. D. Eisner, M. Azzouzi, Z. Fei, X. Hou, T. D. Anthopoulos, T. J. S. Dennis, M. Heeney and J. Nelson, *J. Am. Chem. Soc.*, 2019, **141**, 6362–6374.
- 90 J. Benduhn, K. Tvingstedt, F. Piersimoni, S. Ullbrich, Y. Fan, M. Tropiano, K. A. McGarry, O. Zeika, M. K. Riede, C. J. Douglas, S. Barlow, S. R. Marder, D. Neher, D. Spoltore and K. Vandewal, *Nat. Energy*, 2017, **2**, 1–6.
- 91 G. Garcia-Belmonte, P. P. Boix, J. Bisquert, M. Lenes, H. J. Bolink, A. La Rosa, S. Filippone and N. Martín, *J. Phys. Chem. Lett.*, 2010, **1**, 2566–2571.
- 92 F. Urbach, *Phys. Rev.*, 1953, **92**, 1324.
- 93 Z. Zhang, Y. Li, G. Cai, Y. Zhang, X. Lu and Y. Lin, *J. Am. Chem. Soc.*, 2020, **142**, 18741–18745.